Université Pierre et Marie Curie
Paris VI

Habilitation à diriger des recherches

Speciality: Applied mathematics

presented by

Ionut Danaila

Vortices in fluids and superfluids: a numerical exploration

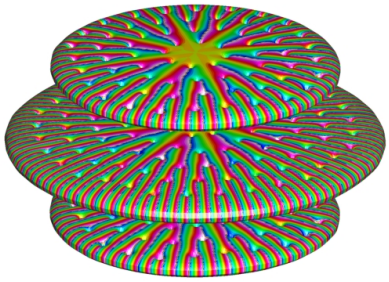

Dissertation publicly presented on December 4, 2008 in front of the Jury:

C. F. Barenghi	**(referee)**	**(Newcastle University, UK)**
P. Comte	**(referee)**	**(Université de Poitiers)**
G.-H. Cottet		**(Université Joseph Fourier, Grenoble)**
J. Dalibard		**(CNRS, Laboratoire Kastler Brossel)**
Q. Du	**(referee)**	**(Pennsylvania State University, USA)**
F. Hecht		**(Université Pierre et Marie Curie)**
B. Maury		**(Université Paris Sud)**
S. Serfaty		**(Université Pierre et Marie Curie)**

Note for the reader: how to use the PDF file of this document

This report was organized as a working document, entirely navigable by the insert of hyperlinks. The PDF file allows to easily navigate in different parts of the report: it is possible to retrieve an equation, a bibliographic reference, or to be directly connected to a Web site. The hyperlinks appear in red in the PDF file. The PDF distribution also offers the possibility to visualize (inside the PDF file) several animations that better illustrate the presented results than usual static images.

Downloading : the PDF file could be downloaded at the address:
http://www.ann.jussieu.fr/~danaila/zdownload/hdr_ionut_EN.pdf

If you want to see the movies too, please download the complete distribution:
http://www.ann.jussieu.fr/~danaila/zdownload/hdr_all_EN.tar.gz
or
http://www.ann.jussieu.fr/~danaila/zdownload/hdr_all_EN.zip

After decompressing the archive files, two folders will be obtained: **danaila_hdr_EN** containing the main file **hdr_ionut_EN.pdf** and the folder **danaila_hdr_films** containing the films.

You have to open now the main file **hdr_ionut_EN.pdf** with Acrobat Reader (Adobe Systems Incorporated).

Navigation : the links appear in red in the PDF file.

The best lecture of the PDF file is offered by Acrobat Reader, starting with version 6. The navigation is greatly facilitated if the buttons *Previous view* and *Next view* are present in the toolbar of Acrobat Reader. Since this is not the case for the default configuration, these buttons could be added from the menus:
View → *Toolbars* → *Add toolbars* → *Page navigation toolbars*.

These buttons allow to easily resume the lecture of the report, after the jump to a bibliographic reference for instance.

Animations/Films: The figure caption starting with the keyword *Animation* indicates that a movie could be played by a simple click on the image. In order to facilitate the lecture, the movies are played inside the PDF file. There is one exception: the movie at page 15 will be opened in an external viewer.

These features of the electronic version of the report were successfully tested on Windows XP and Mac OS with Acrobar Reader 8.

Summary

This report presents research activities that I have been developing since my arrival in Laboratoire Jacques-Louis Lions in 1999. My contributions are mainly in the scientific computing field, with two major application domains: the simulation of *classical* fluid flows and the simulation of superfluids (Bose-Einstein condensates).

Each application theme is presented in a devoted part of the report, with its own final chapter describing the work in progress and the specific research project. Chapter titles mention not only the considered application, but also the specific numerical methods developed for this purpose. Since a rich variety of problems are presented, the bibliographic references are organized separately for each chapter, in the third part of the report.

This report was conceived as a working document, with self-containing chapters. Each chapter starts with an introductory record card summarizing the motivations, the scientific context and the main obtained results; the keywords describing the activity, the corresponding papers and scientific collaborations are also mentioned. The presentation is intended to both specialists and readers looking to more general information on the topic announced in the title. The inserts in text contain technical information and is not compulsory to follow the general presentation.

My vision on scientific computing is that each physical problem requests specific numerical tools. This explains the variety of the numerical developments presented in this report. Numerical methods or algorithms were often taken from a general theoretical analysis to the implementation on large 3D numerical codes used for the simulation of more or less realistic problems. Transposing difficult real problems into a more academic framework was also worthwhile in bringing useful information on less documented cases. A particular attention was devoted to the physical interpretation of the obtained numerical results. It is my intimate conviction that the greatest satisfaction in scientific computing is to transform the computer into a reliable experimental device reproducing real physics.

The last point that I should like to emphasize here is the importance that I grant in passing the results of the research activity into teaching. To this purpose, I had the pleasure to write together with my colleagues, F. Hecht, O. Pironneau, M. Postel, P. Joly et S. M. Kaber, three text books in which some of the developed numerical methods are presented in a simplified framework.

The following paragraphs give an overview of the topics presented in each chapter. The quest for vortex structures in all simulated systems may be regarded as the general guideline of the presentation.

• The first part is devoted to the description of numerical simulations of classical fluid flows.

The round jet flow, with typical vortex structures appearing in the near field, is the main topic of **Chapter 1**. Spectral elements and finite differences methods are used to solve the incompressible Navier-Stokes equations in three-dimensions. The ideas behind each method is briefly recalled. Numerical results allow to introduce a first family of vortices (or coherent structures): vortex rings, streamwise vortices and helical vortices. The combination of such vortex structures, assimilated to unstable modes in stability theories, resulted in a model used to simulate a particular class of jet flows (bifurcating, blooming and flapping jets) with spectacular increasing of the spreading angle.

Chapter 2 introduces numerical and theoretical tools for numerically solving the compressible Navier-Stokes equations. In particular, a fictitious domain method is presented for the simulation of flows with obstacles or moving walls embedded in the computational domain. The method, based on a immersed boundary methodology, was tested on academic cases, as the simulation of the flow in a compression squared machine and the interaction of vortex dipoles with obstacles. New vortex structures will be thus introduced: the tumble vortex and the vortex dipole. The chapter also presents more applied research activities, developed in collaboration with industrial partners: modeling and simulating real injection conditions in an engine and numerical evaluation of the behaviour of some industrial codes (AVBP, IFP-C3D).

Chapter 3 describes my main research activity in the simulation of classical fluids: the development of numerical solvers for the incompressible or low-Mach number Navier-Stokes equations, using cylindrical coordinates. The finite differences method used in my code called JETLES (JET Large Eddy Simulations) is described in great detail. Numerical contributions to the study of the flow dominated by vortex rings are presented as applications. This flow is relevant for the industrial flow that is created when the fuel is injected in internal combustion engines.

The first part of the report is closed in **Chapter 4** that outlines the work in progress and my future plans in the field of the numerical simulation of classical flows. These concern the mathematical and numerical analysis of ideal vortex ring models, the numerical and theoretical analysis of the pipe-flow in the entry region, and further numerical developments of the JETLES code for the simulation of conical injection in internal combustion engines.

• The second part of the report presents my very recent activities in the simulation of superfluid systems, namely the Bose-Einstein condensate (BEC). This part is divided in three chapters.

Chapter 5 introduces the physical problem and the experimental BEC configurations with vortices studied in École Normale Supérieure (ENS) group. The mathematical model for quantized vortices is also described, since different from that used for vortices in classical fluids. The numerical code developed to simulate equilibrium states of 3D BEC with vortices is described in detail. This code was called BETI (Bose-Einstein Temps Imaginaire), since the imaginary time propagation of the Gross-Pitaevskii equation is its basic principle. This is one of the few existing 3D numerical codes used for the study of the physics of BECs.

The main results obtained using the numerical code BETI are shown in **Chapter 6**. I describe in detail the three-dimensional structure of vortices for different trapping potentials used in experiments. The simulations offer a detailed 3D picture of vortex configurations that is not available from experiments and 2D simulations. A particular attention was devoted to the physical interpretation of the results by using post-processing diagnostics close to experimental ones. Numerical data are always compared to available experimental and theoretical results and a remarkably good qualitative and quantitative agreement is found.

In **Chapter 7** I briefly present the undergoing studies of new BEC configurations, as the rotating BEC in one-dimensional optical lattices. These systems, in which the initial cigar-shape condensate is divided in several quasi-2D condensates, start to be studied experimentally. Further developments of the BETI code are also mentioned.

• The third part gathers the bibliographic references of each chapter.

Publications

The electronic versions (PDF files) of the publications can be downloaded from my personal Web page

http://www.ann.jussieu.fr/~danaila

menu *Papers*.
Titles appearing in red are direct links to the PDF files on my Web page.

Books

[O1] I. Danaila, P. Joly, S. M. Kaber, M. Postel
An Introduction to Scientific Computing. Twelve Computational Projects Solved with MATLAB., **Springer**, 2007.

[O2] I. Danaila, P. Joly, S. M. Kaber, M. Postel
Introduction au calcul scientifique par la pratique. 12 projets résolus avec Matlab., **Dunod**, Collection Science Sup : Masters et Ecoles d'Ingénieurs, Paris, 2005.

[O3] I. Danaila, F. Hecht, O. Pironneau
Simulation numérique en C++, **Dunod**, Collection Science Sup : Masters et Ecoles d'Ingénieurs, Paris, 2003.

[O4] Co-éditeur avec A. Blouza, S. M. Kaber, P. Joly, B. Luquin, F. Murat et M. Postel des **Actes du 23ème Congrès national d'analyse numérique**, ESAIM Proceedings, vol XI, EDP Sciences, Paris, 2002.

Articles

[A1] I. Danaila, J. Hélie
Numerical simulation of the postformation evolution of a laminar vortex ring, **Physics of Fluids**, **20**, p. 073602(1–14), 2008.

[A2] S. Benteboula, I. Danaila
Variable density vortex rings,
publié dans **Advances in Turbulence XI**,
Editors J. M. L. M. Palma and A. Silva Lopes, Springer, p. 771, 2007.

[A3] I. Danaila
Three-dimensional simulations of quantized vortices in rotating Bose-Einstein condensates, **Bulletin of the "Politehnica" University of Timisoara, Transactions on Mechanics**, **51**, p. 155-162, 2006.

[A4] S. Benteboula, I. Danaila
Simulation numérique de l'injection gaz-gaz à masse volumique variable, publié dans **Défis thermiques dans l'industrie nucléaire**, Editions Société Française de Thermique, p. 521-525, 2006.

[A5] O. El Ganaoui, C. Habchi, G. Bruneaux and I. Danaila
Numerical simulation of an experimental gas-gas jet generated by single-hole diesel-like injectiont,
Int. J. Numer. Meth. Fluids, **47**, p. 1011-1018, 2005.

[A6] I. Danaila
Three-dimensional vortex structure of a fast rotating Bose-Einstein condensate with harmonic-plus-quartic confinement,
Physical Review A, **72**, p. 013605(1-6), 2005.

[A7] A. Aftalion, I. Danaila
Giant vortices in combined harmonic and quartic traps,
Physical Review A, **69**, p. 033608(1-6), 2004.

[A8] I. Danaila
Vortex dipoles impinging on finite aspect ratio rectangular obstacles,
Flow, Turbulence and Combustion, **72**, p. 391-406, 2004.

[A9] L.-C. Crasovan, V. M. Pérez-García, I. Danaila, D. Mihalache and L. Torner
Three-dimensional parallel vortex rings in Bose-Einstein condensates,
Physical Review A, **70**, p. 033605(1-5), 2004.

[A10] A. Aftalion, I. Danaila
Three-dimensional vortex configurations in a rotating Bose Einstein condensate, **Physical Review A 68**, p. 023603(1-6), 2003.

[A11] I. Danaila
Numerical simulation of a rotating Bose Einstein condensate,
publié dans **Actes du CANUM**, 2003.

[A12] I. Danaila, B. J. Boersma
Direct numerical simulation of bifurcating jets,
Physics of Fluids, **12 (5)**, p. 1255–1258, 2000.

[A13] I. Danaila, T. Baritaud
Direct numerical simulation of IC engine flows using a boundary body-force method, publié dans **Actes du CANUM**, 2000.

[A14] I. Danaila, J. Dusek, F. Anselmet
Nonlinear dynamics at a Hopf bifurcation with axisymmetry breaking in a jet, **Physical Review E**, **57 (4)**, p. 3695–3698, 1998.

[A15] I. Danaila, B. J. Boersma
Mode interaction in a forced homogeneous jet at low Reynolds numbers,
publié dans *Proceedings of the Summer Program 1998*, Center for Turbulence Research, Stanford University and NASA Ames, p. 141–158, 1998.

[A16] I. Danaila, J. Dusek, F. Anselmet
Nonlinear dynamics of Low Reynolds Number Round Jets: Periodic Attractors and Transition to Chaos,
publié dans **Advances in Turbulence VII**,
Editor U. Frisch, Kluwer Academic Publishers, p. 105–108, 1998.

[A17] I. Danaila, J. Dusek, F. Anselmet
Coherent structures in a round, spatially evolving, unforced, homogeneous jet at low Reynolds numbers,
Physics of Fluids, **9 (11)**, p. 3323–3342, 1997.

[A18] I. Danaila, J. Dusek, F. Anselmet
Direct numerical simulations of the free, unsteady, round, unforced jet at low Reynolds numbers,
publié dans **Direct and Large-Eddy Simulation II**, Editors J.-P. Chollet, P. R. Voke and L. Kleiser, Kluwer Academic Publishers, p. 1–10, 1997.

[A19] I. Danaila, J. Dusek, F. Anselmet
Space Structure of the Free, Unsteady, Round, Homogeneous Jet at Low Reynolds Numbers,
publié dans **Advances in Turbulence VI**, Editors S. Gavrilakis, L. Machiels and P. A. Monkewitz, Kluwer Academic Publishers, p. 11–14, 1996.

[A20] J. Dusek, Ph. Fraunié, C. Dauchy, I. Danaila
Secondary instabilities and transition to turbulence in wakes and jets, publié dans **Computation of Three-Dimensional Complex Flows**, Editors M. Deville, S. Gavrilakis and I. L. Ryhming, Vieweg, Braunschweig/Wiesbaden, p. 78–87, 1996.

Numerical codes

[Code 1] Code **BETI** Origin: 3D code written from scratch,
Equations: non-linear Schrödinger (imaginary time propagation),
Method: finite differences, compact schemes,
Scheme: Runge-Kutta + Crank-Nicolson ,
Applications: 3D simulation of rotating Bose-Einstein condensates, 3D structure of quantized vortices.

[Code 2] Code **JETLES** Origin: 3D code written from scratch,
Equations: incompressible Navier-Stokes, cylindrical coordinates,
Method: second order finite differences, staggered grids,
Scheme: Runge-Kutta + Crank-Nicolson,
Turbulence model: direct and large numerical simulation,
Applications: axisymmetric and 3D round jets, vortex rings.

[Code 3] Code **NTMIX-BF** Origin : the NTMIX code of IFP,
Equations: compressible Navier-Stokes, Cartesian coordinates,
Method: finite differences, compact schemes,
Scheme: Runge-Kutta
Turbulence model: direct and large numerical simulation,
Applications: 2D et 3D engine flows, vortex dipoles.

Scientific illustrations

[V1] The film (1.1) on the vortex pairing in a round jet was selected for the last edition of the CDrom *Multimedia Fluid Mechanics*, Cambridge University Press, 2008.

[V2] Images of quantized vortices in Bose-Einstein condensates (see chapter 6) are used as illustration in the recent book by A. Aftalion, *Vortices in Bose-Einstein Condensates*, Birkhäuser, 2006.

[V3] The image of a giant vortex in rotating Bose-Einstein condensates is on the cover of the special issue *Bose Einstein condensates : recent advances in collective effects*, CRAS de Physique, 2004.

[V4] A bifurcating jet image (1.6) is used as illustration in the book by P. Durbin and B. Pettersson Reif, *Statistical Theory and Modeling of Turbulent Flows*, John Wiley & Sons, 2000.

Technical reports

[R1] I. Danaila
Code JETLES. Simulations numériques directes (DNS) et des grandes échelles (LES) des écoulements incompressibles en coordonnées cylindriques. Manuel du code JETLES, UPMC, 2008.

[R2] I. Danaila, S. Benteboula : *Etude numérique et théorique des structures tourbillonnaires dans une injection gaz-gaz. Simulations numériques directes avec les codes JETLES et AVBP.*, Rapport de contrat UPMC/Institut Français du Pétrole, 2004.

[R3] M. Ballestra, I. Danaila : *Etude numérique de la formation et de la dissipation des tourbillons créés par un jet conique monophasique,* Rapport de contrat UPMC/Institut Français du Pétrole, 2002.

[R4] I. Danaila : *Numerical Implementation of the Body-Force Method in the NTMIX Code*, Rapport interne de l'Institut Français du Pétrole, 2001.

[R5] I. Danaila, T. Baritaud
Large Eddy Simulations for Stratified Charge Engines. LES Engines Program. Twelve-months periodic report. Institut Français du Pétrole, March 1999.

Contents

I

Simulation of classical fluid flows

1. Spectral elements and finite differences methods for the incompressible Navier-Stokes equations: three-dimensional simulations of round jets

General presentation

This chapter presents my very first numerical simulations, performed during my PhD and in the first two years after my arrival to Laboratoire Jacques-Louis Lions. It is helpful to show these results since they triggered subsequent numerical work (presented in the next two chapters).

The near-field evolution of a round jet was simulated using either spectral elements methods (PhD work, Danaila, 1997) or finite differences methods (Danaila and Boersma, 2000) to solve the incompressible Navier-Stokes equations in 3D. At the beginning of this activity, most of the numerical simulations of round jets were based on a *temporal* model, assuming periodic boundary conditions in the streamwise direction. My results were among the first direct numerical simulations (DNS) using inflow/outflow boundary conditions to capture the evolution in time and space of the 3D jet flow.

The numerical and theoretical tools developed during my PhD will be briefly presented. They will allow to introduce a first family of vortices (or coherent structures), typical for the round jet flow: vortex rings, streamwise vortices and helical vortices. The gallery of vortices will be completed in the next chapters.

My PhD work was followed by several research activities related to the development of two new numerical codes, more effective when dealing with 3D round jet flows. Both codes use finite differences schemes and projection methods for the incompressible Navier-Stokes equations. I present in this chapter some results obtained with the code using spherical coordinates. This code, provided by B. J. Boersma (TU Delft), was used to investigate strategies to control the round jet. Spectacular

evolutions (bifurcating of flapping jets) were observed when appropriate forcing was imposed at the inlet.

The second code, that I have been developing since 1998, is based on a discretization of the Navier-Stokes equations in cylindrical coordinates. The numerical method used in this code will be presented in chapter 3.

Key words:	spectral elements, finite differences, incompressible Navier-Stokes equations, 3D simulation, round jet, weakly non-linear stability, Landau model.
Publications :	articles : [A12], [A15] (during my PhD) : [A14], [A17], [A16], [A18], [A19], [A20].
Collaborations :	B. J. Boersma (Delft University, The Netherlands), D. Parekh (Georgia Tech, USA), my PhD advisors F. Anselmet (IRPHE, Marseille), J. Dušek (Université Louis Pasteur, Strasbourg).

1.1. Spectral elements method and weakly nonlinear stability for the study of round jet instabilities

During my PhD I had the opportunity to use an academic version of the NEKTON code, originally developed by Tony Patera (Patera, 1984). This code became a commercial package and, to my knowledge, finally disappeared from the very competitive world of Navier-Stokes commercial solvers.

NEKTON allowed fully 3D simulations using spectral elements methods to solve the incompressible Navier-Stokes equations. The code was very effective in the simulation of flow instabilities since its local (within one element) spectral accuracy permitted to capture very disparate length scales in different regions of the flow.

Since the spectral elements methods is not largely used for flow simulations (compared to finite volumes, finite elements or finite differences), it could be helpful to remind here the main characteristics of the method. The computational domain ($\Omega \subset \mathbb{R}^n$) is filled with 3D Lagrangian elements $(\mathcal{E}_k)_{k=1\ldots K}$. Only the C^0 continuity is imposed, bringing about a drawback in the form of discontinuities of the velocity field derivatives at element interfaces. Local basis functions are high order polynomials ($N \geq 5$):

$$\phi_{pql}^{(\mathcal{E}_k)} = h_p(\xi)\, h_q(\eta)\, h_l(\zeta),\ h \in \mathcal{P}_N \implies u(x,y,z)|_{(\mathcal{E}_k)} = \sum_{p,q,l=0}^{N} \widehat{u}_{pql}^{k}\, \phi_{pql}^{(\mathcal{E}_k)},$$

where local coordinates (ξ, η, ζ) correspond to the transformation of each element into the cube $[-1, 1]^3$. The collocation points are uniformly distributed on each side of the element and form an orthogonal grid. The approximation error is of order of $\mathcal{O}[K^{-N}\, exp(-ct. \cdot N)]$ (see also Neitzel et al., 1995; Henderson and Karniadakis, 1995). The best strategy to obtain a good numerical approximation is to use relatively large spectral elements and very high order polynomials as basis functions. The high accuracy of spectral methods and the flexibility of the finite elements are thus used for the simulation.

The originality of the numerical approach used in this study was the spontaneous destabilization of the jet flow by the numerical noise. This noise is introduced at the interface of the elements modeling the jet nozzle, where the velocity has a jump and

the pressure gradient is discontinuous. Similar random noise exists in experimental devices.

Since the simulated jet flow is spontaneously destabilized without any forcing, we could observe different coherent structures appearing naturally in the near field region of the jet. A Fourier decomposition of the flow field allowed the extraction of the unstable modes and the identification of the coherent structures resulting from their interaction. The evolution in time and space of these structures was carefully analyzed. The parameter of the study was the Reynolds number, defined as $Re = V_0\, D/\nu < 500$, where V_0 is the injection velocity, ν the kinematic viscosity of the fluid, and D the diameter of the nozzle.

For high Reynolds numbers ($Re = 500$), the *classical* scenario of the jet evolution is found in the simulation: Kelvin-Helmholtz instability, roll-up of vortex rings, vortex pairing (see animation 1.1), secondary instability with streamwise vortices appearing in the flow. The break-up of coherent structures was put into evidence as the last stage before the chaotic and turbulent state (see Danaila et al., 1996a, 1997a,b).

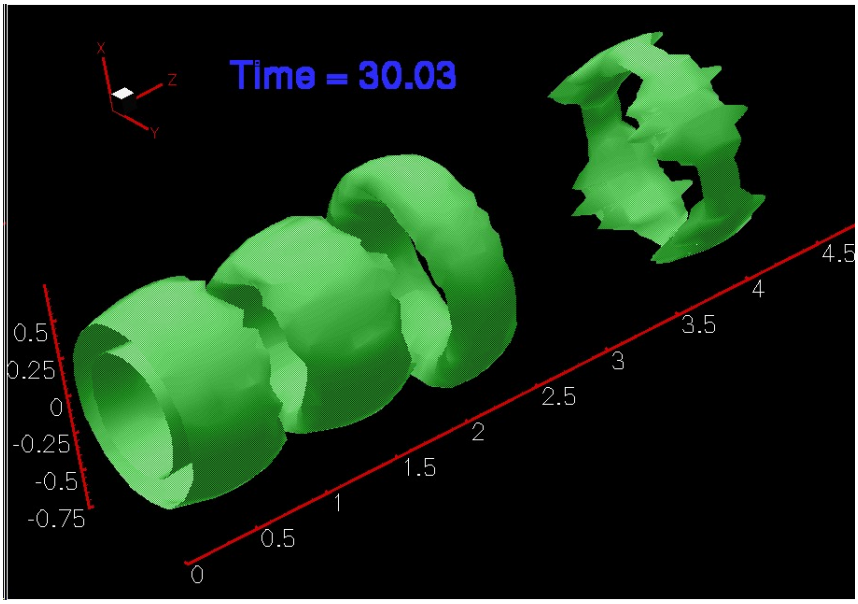

Figure 1.1.: (Animation) Numerical simulation of the pairing of vortex rings in the near field of a round jet. This film was selected for the new edition of the *Multimedia Fluid Mechanics* (Homsy, 2008).

For very low Reynolds numbers, the flow field is dominated by the two counter–rotating helical modes (Fig. 1.2). This change of topology with the Reynolds number, already reported in experimental studies, was found for the first time by means of direct numerical simulations (Danaila et al., 1997a).

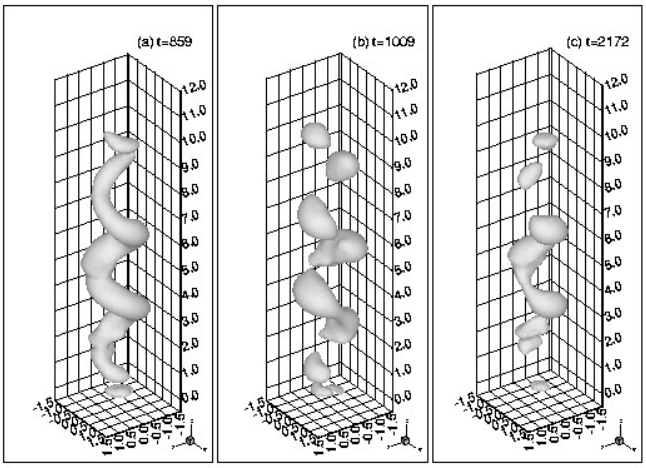

Figure 1.2.: Superposition of counter-rotating helical modes in a round jet.

From a mathematical point of view, we had to deal with the very interesting problem of the degeneracy of the spectrum of the linearized Navier-Stokes equations. More in detail, writing the Navier-Stokes equations in cylindrical coordinates (r, θ, z) (the complete form of these equations is given in chapter 3) and linearizing around an axisymmetric base-flow, we obtain the following operator

$$\nabla^2_{m^2} = \frac{1}{r}\frac{\partial}{\partial r} r \frac{\partial}{\partial r} + \frac{\partial^2}{\partial z^2} - \frac{m^2}{r^2}, \tag{1.1.1}$$

that depends on the square of the azimuthal wavenumber m. This means that, if an eigenvalue $\lambda(m^2)$ exists for $m \neq 0$, there are two linearly independent eigenvectors $\Phi_{\pm|m|} = \phi_{\pm|m|} \exp(\mp i|m|\theta)$. The result suggests that when the flow is dominated by a helical mode $m \neq 0$, its counter-rotating pair is present as well. This is the case for the round jet dominated by helical modes $m = \pm 1$ (Fig. 1.2).

The flow field decomposition (see, for instance Van Dyke, 1975; Carte et al., 1995) was added to the original code to calculate during the simulation the Fourier components of the velocity field for each time period $T = 2\pi/\omega$ of the primary instability:

$$\mathbf{v} - \mathbf{V} = \widetilde{\mathbf{v}}'(r, \theta, z; t, s)|_{s=t} = \sum_{n=-\infty}^{\infty} \mathbf{c}_n(., s) e^{in\omega t}, \quad \text{with } \mathbf{c}_n = \overline{\mathbf{c}}_{-n}. \tag{1.1.2}$$

In the previous decomposition, the new time scale s will capture the slow evolution of the amplitude of the rapid oscillations of period T. An interesting idea (see also Dušek et al., 1994; Carte et al., 1995) was to replace the original Navier-Stokes equations by a set of evolution equations for the Fourier coefficients $\mathbf{c}_n$ (depending on s and space variables). In the round jet case, the fluctuating field corresponding to the most unstable mode was:

$$\widetilde{\mathbf{v}}'(r, \theta, z; t, s) = \left[A_+(s)\,\phi_+(r, z)\,e^{-i\theta} + A_-(s)\,\phi_-(r, z)\,e^{i\theta}\right] e^{i\omega t}. \tag{1.1.3}$$

Using the periodicity in the azimuthal θ direction, we finally calculated the fluctuating field by a double Fourier decomposition:

$$\mathbf{v}'(r,\theta,z;t,s) = \sum_{n=-\infty}^{\infty}\sum_{l=-\infty}^{\infty} \mathbf{c}_{n,l}(r,z,s)e^{in\omega t}\,e^{-il\theta}, \quad \text{with } \overline{\mathbf{c}_{n,l}} = \mathbf{c}_{-n,-l}. \tag{1.1.4}$$

The analysis of the evolution of the Fourier coefficients resulted in a weakly nonlinear theory for the interaction of the two counter–rotating helical modes ($m = \pm 1$). The final Landau-type model (Danaila et al., 1998a,b) described the evolution of the complex amplitudes of the two helical modes:

$$\begin{cases} \dfrac{\partial \widetilde{A}_+}{\partial s} = \gamma\widetilde{A}_+ - \widetilde{A}_+(\widetilde{C}|\widetilde{A}_+|^2 + \widetilde{D}|\widetilde{A}_-|^2) - \widetilde{A}_+(\widetilde{a}|\widetilde{A}_+|^4 + \widetilde{b}|\widetilde{A}_+|^2|\widetilde{A}_-|^2 + \widetilde{c}|\widetilde{A}_-|^4), \\ \dfrac{\partial \widetilde{A}_-}{\partial s} = \gamma\widetilde{A}_- - \widetilde{A}_-(\widetilde{C}|\widetilde{A}_-|^2 + \widetilde{D}|\widetilde{A}_+|^2) - \widetilde{A}_-(\widetilde{a}|\widetilde{A}_-|^4 + \widetilde{b}|\widetilde{A}_-|^2|\widetilde{A}_+|^2 + \widetilde{c}|\widetilde{A}_+|^4). \end{cases} \tag{1.1.5}$$

The coefficients of the model could be expressed from Navier-Stokes equations. For the round jet instabilities dominated by helical modes, the theoretical predictions were very well supported by the results of direct numerical simulations (Fig. 1.3). It is interesting to note that the theoretical framework based on the competition of two unstable modes arising as a result of a degenerated linear spectrum is of a more general interest and could be applied for the study of different flows (e.g. the wake behind a sphere).

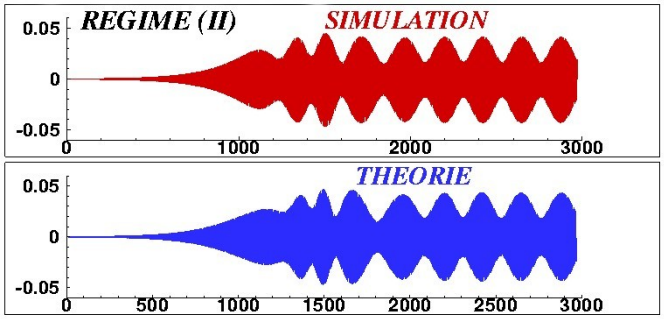

Figure 1.3.: Round jet flow dominated by the two counter-rotating helical modes $m = \pm 1$. Theoretical reconstruction of the azimuthal velocity signal and comparison with the signal provided by the direct numerical simulation. The oscillation period being very small, only the envelope of the signal is visible.

1.2. Finite differences method for Navier-Stokes equations in spherical coordinates: bifurcating, blooming and flapping jets

The analysis developed during my PhD was used in a research project on a particular class of jets: bifurcating and blooming jets. Bifurcating jets, which split into two distinct branches, are of particular interest for many practical applications, due to their increased spreading angle and mixing properties. Such flows were experimentally obtained (Lee and Reynolds, 1985; Parekh et al., 1988) by mechanically forcing the flow at the jet nozzle. Figure 1.4 shows the spectacular evolution of what was called a *blooming* jet. A recent review (Reynolds et al., 2003) describes in detail these experiments.

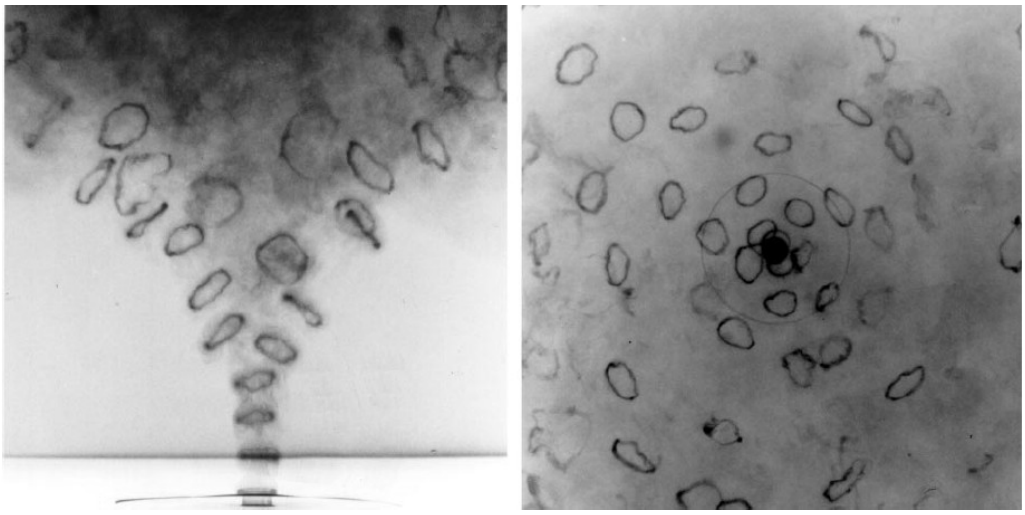

Figure 1.4.: *Blooming* jet obtained experimentally by Lee and Reynolds (1985).

This research activity was initiated during the *Summer Program 1998* in Center for Turbulence Research, Stanford University. This was also the starting point of a nice collaboration with B.J. Boersma from TU Delft, The Netherlands. He provided a 3D incompressible Navier-Stokes numerical code using spherical coordinates. I continue to use this finite differences code and adapt it to new configurations (see also chapter 3).

The idea to use spherical coordinates for the round jet simulations is quite original. The computational domain (Fig. 1.5) results from the intersection between the shell defined by two surfaces ($r = const$) and the cone starting from the center of the sphere with a fixed opening angle. Such a discretization is able to follow the streamwise spreading of the jet and allows a well-balanced resolution of the flow field with a reasonable number of grid points. Besides, the code, using an explicit

integration scheme, is parallel and make possible direct numerical simulation of turbulent jets also.

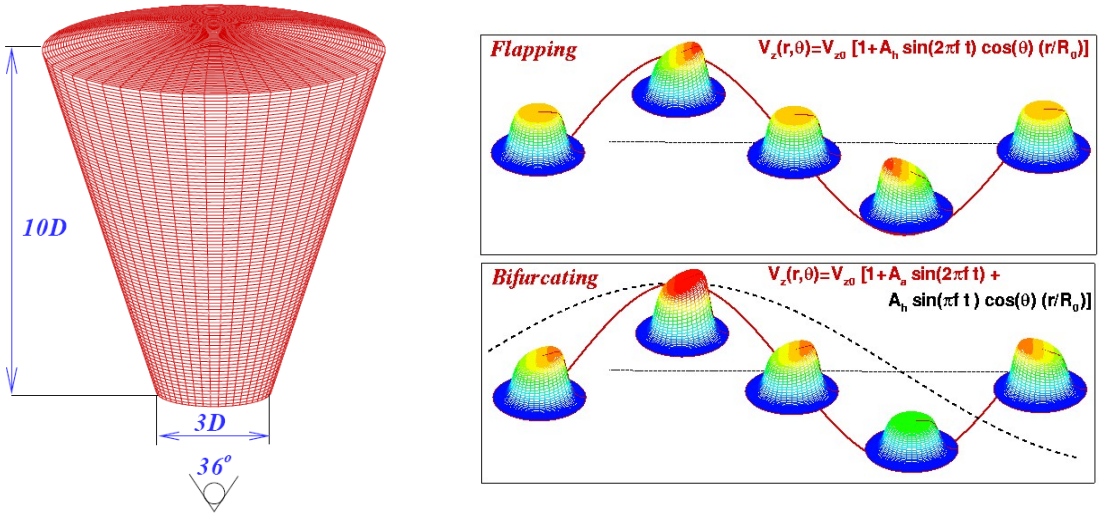

Figure 1.5.: Finite differences method in spherical coordinates. Computational domain and examples of forcing applied at the jet nozzle to control the jet flow.

Starting from a linear stability analysis, we have established different analytical forms for the disturbances (Fig. 1.5) that have to be applied at the jet nozzle in order to obtain bifurcating jets. The model is based on the superposition of the most unstable modes in the jet (the axisymmetric $m = 0$ and the counter-rotating helical modes $m = \pm 1$):

$$V_z = 1 + \sum_{m0,\pm 1} A_m sin\left(2\pi f_m t - m\theta_c + \Phi_m\right)\left(\frac{2r_c}{D}\right)^{|m|}. \qquad (1.2.1)$$

The frequencies for individual modes came from linear stability analysis. With this model, we could numerically reproduce the spectacular evolution (Fig. 1.6) observed experimentally for such jets (Parekh et al., 1988). New forcing forms (*flapping* excitation), not explored experimentally, were proved to trigger bifurcating jets (Danaila and Boersma, 1998, 2000).

The optimization of the parameters defining the forcing (1.2.1) was studied in Hilgers and Boersma (2001). It should be noted that the investigation of bifurcating jets is still topical – see the recent review of Reynolds et al., 2003 and new experiments of Suzuki et al., 2004. Besides, Navier-Stokes numerical simulation of blooming jets are not, to my knowledge, available in the open literature – this is a nice computational case that I intend to tackle one day!

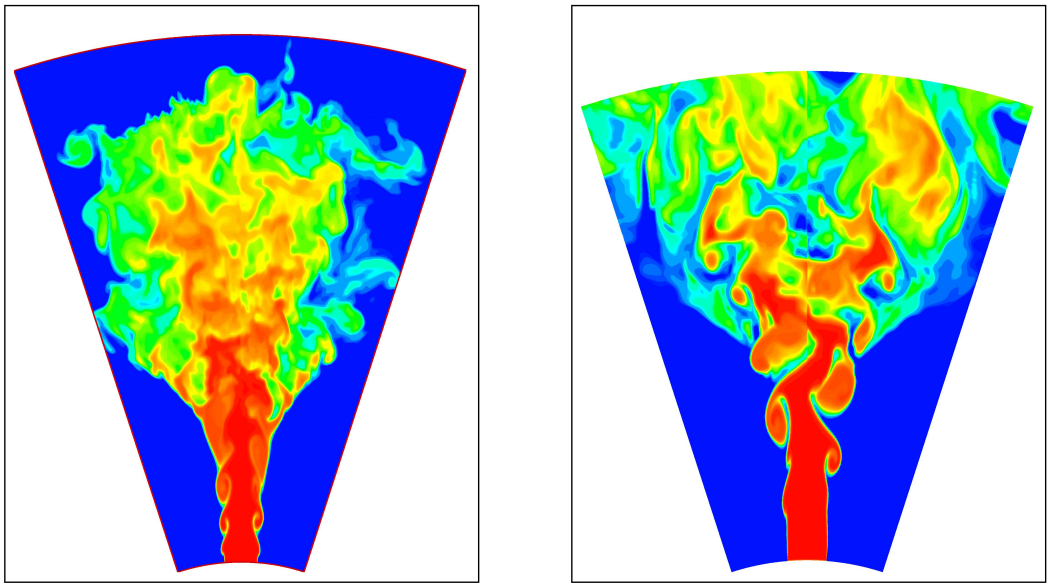

Figure 1.6.: Bifurcating (left) and flapping (right) jets obtained numerically. A similar image from Danaila and Boersma (1998) was used as illustration in the book by Durbin and Pettersson Reif (2000).

2. Direct and large eddy simulations of internal combustion engine flows

General presentation

This activity started in 1998 with my post-doctoral research in Institut Français du Pétrole (IFP) and continued several years by concluding with IFP two research contracts on numerical simulations of flows developing in internal combustion engines. I have also co-advised in this framework a post-doc (O. El Ganaoui) and a master-degree (M. Ballestra) research activities taking place at IFP.

I present in this chapter only the numerical tools developed for the compressible Navier-Stokes equations. In particular, I developed and implemented in an IFP code a fictitious domain method allowing the simulation of obstacles or moving walls. The method based on an immersed boundary methodology was tested on academic cases, as the simulation of the flow in a compression squared machine (Danaila and Baritaud, 1999; Danaila, 2001), and the interaction of vortex dipoles with obstacles (Danaila, 2004). New vortex structure will be thus introduced: the tumbling vortex and the vortex dipole.

The collaboration with IFP researchers also gave me the opportunity to work on more *industrial* topics, as modeling and simulating real injection conditions in an engine (El Ganaoui et al., 2005), and the numerical evaluation of the behaviour of industrial codes, as AVBP and IFP-C3D on well defined academic cases (Danaila and Benteboula, 2004).

In connection with this activity I have also developed a new numerical code for the incompressible Navier-Stokes equations in cylindrical coordinates – this will be presented in chapter 3.

Key words: finite differences, compact schemes, compressible Navier-Stokes equations, immersed boundary, body force, internal combustion engines, vortex dipole.

Publications :	articles	: [A5], [A8], [A13],
	reports	: [R2], [R4], [R5]
	numerical codes	: [Code3].
Collaborations :	C. Habchi, T. Baritaud, C. Angelberger (Institut Français du Pétrole), O. El Ganaoui (Peugeot PSA), T. Poinsot (CERFACS).	

2.1. Immersed boundary and finite differences methods for compressible Navier-Stokes equations

Numerical simulations of industrial flows must usually cope with complex geometries. Moving boundaries and multi-body geometries are other factors increasing the complexity of the numerical method. Currently, the most widely used method for simulating industrial configurations involves unstructured mesh techniques (see figure/animation 2.1). This approach is very powerful for arbitrarily complex geometries, but encounters some difficulties when dealing with moving boundaries. Global or local remeshing that preserves boundaries and avoids mesh skewness is necessary, and therefore, increased computer resources are required. The structured mesh approach can use multi-block domains to simulate complex geometries. Local body-fitted curvilinear coordinates are used to reproduce the shape of individual components of the geometry.

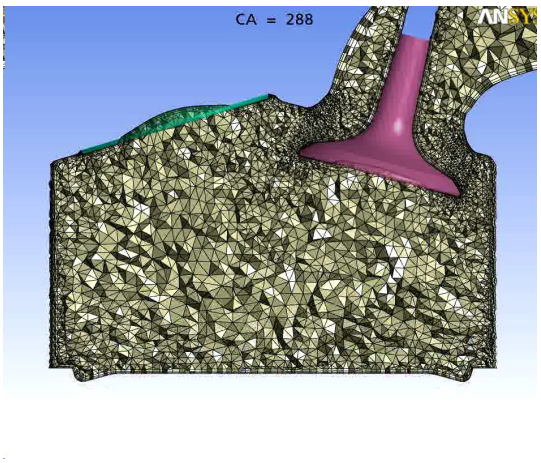

Figure 2.1.: (Animation) Mesh for the industrial computation of engine flows (courtesy of J. Hélie, Continental Automotive France).

Moving bodies can be simulated by mesh embedding techniques, as *Chimera* (see Steger et al., 1983) or *FAME* (flexible mesh embedding techniques) (see Albone, 1992). The mesh associated to the body moves with it, while the background mesh remains unchanged. Interpolation on the overlapping meshes and storage of the curvilinear metrics for each block are the main drawbacks of the method. The method is very time consuming since the efficiency of the basic flow solver is dramatically reduced.

A third possibility consists in using a completely Cartesian fixed mesh and fictitious domain techniques. Among these methods, the *immersed boundary* approach, introduced by C. S. Peskin in his PhD in 1972 to simulate the blood flow in the human heart (see also **?**), has recently been regaining popularity. Several versions of the method for different applications have been published (for a recent review, see Mittal and Iaccarino, 2005).

The general idea of the method is very simple: the solid bodies are immersed in the computational domain and mimicked by the forces of pressure and shear that exist along the body surface. The initial solver can thus be used on the entire computational domain, that keeps a simple global shape embedding complicated or moving bodies. The question of how modifying the initial evolution equations is answered differently in the numerous versions of the method.

I have used a particular method, called the *body-force* method, which explicitly prescribes the force acting on the fluid flow due to the presence of the solid body. Suitable volume forces ($\mathbf{f}$) are numerically introduced as source terms in the Navier-Stokes equations. These forces are such calculated as to yield a controlled value $\mathbf{V}_b$ of the velocity on the surface of the mimicked solid body ($\mathbf{V}_b \neq 0$ for moving bodies). The volume force field acts only inside the body and can be prescribed in several ways (see Saiki and Biringen, 1996; Angot et al., 1999).

I have adapted the body-force method proposed by Mohd-Yosuf (1997) for incompressible flows to the numerical simulation of compressible flows. The method was also implemented in the NTMIX solver developed in IFP. I present in the following the main ideas of the approach, since it can be easily implemented in any Navier-Stokes solver using an explicit time-integration scheme.

The compressible Navier-Stokes equations, written in their general form:

$$\frac{\partial}{\partial t}\begin{pmatrix}\rho\\ \rho\cdot\mathbf{V}\\ \rho e\end{pmatrix}+\mathrm{div}\begin{pmatrix}\rho\cdot\mathbf{V}\\ \rho\cdot\mathbf{V}\otimes\mathbf{V}+p\cdot\vec{\vec{I}}\\ \rho e\cdot\mathbf{V}+p\cdot\mathbf{V}\end{pmatrix}=\begin{pmatrix}0\\ \mathbf{f}\\ \mathbf{f}\cdot\mathbf{V}\end{pmatrix}+\mathrm{div}\begin{pmatrix}0\\ \vec{\vec{\tau}}\\ \vec{\vec{\tau}}\cdot\mathbf{V}-\mathbf{q}\end{pmatrix}, \tag{2.1.1}$$

include a volume source term $\mathbf{f}$, which is generally derived from a potential (e.g. gravity). The idea of the body-force method is to impose such an external force field to mimic the presence of solid bodies. The force field will be thus function of time and space and will act only on the cells corresponding to the modeled body. The procedure introduced by Mohd-Yosuf (1997) uses a discrete *time-derivation* of the forcing to fix the velocity at a desired value. We apply this technique only for the momentum conservation equations. For a generic Runge-Kutta time advancement scheme, one can write the discretized Navier-Stokes equations as:

$$\mathbf{Y}(t_n+\alpha\Delta t)=\mathbf{Y}(t_n)+\beta\Delta t\left[\mathbf{RHS}(t_n)+\mathbf{F}(t_n)\right],\qquad \mathbf{Y}=\rho\mathbf{V}, \tag{2.1.2}$$

where RHS contains the non-linear terms, pressure and viscous terms. If the value $\mathbf{Y}_b=\rho\mathbf{V}_b$ have to be imposed at the time instant $t_n+\alpha\Delta t$, the body force vector will be calculated as:

$$\mathbf{F}(t_n)=\frac{\mathbf{Y}_b(t_n+\alpha\Delta t)-\mathbf{Y}(t_n)}{\beta\Delta t}-\mathbf{RHS}(t_n). \tag{2.1.3}$$

For the compressible formulation, the work of the external force field is added as a source term $\mathbf{f}\cdot\mathbf{V}_b$ in the energy conservation equation (2.1.1).

RK step	time	Compute
0	t_n	initialize
1	$t_n + \frac{1}{4}\Delta t$	$Y^{'} = Y^n + \frac{1}{4}\Delta t\,\mathbf{RHS}_n$ $\Delta t\,\mathbf{F}(t_n + \frac{1}{4}\Delta t) = -\frac{1}{4}\Delta t\,\mathbf{RHS}_n + \left[Y_b(t_n + \frac{1}{4}\Delta t) - Y^n\right]$ $Y^{'} = Y^{'} + \Delta t\,\mathbf{F}(t_n + \frac{1}{4}\Delta t)$
2	$t_n + \frac{8}{15}\Delta t$	$Y^{''} = Y^n + \frac{8}{15}\Delta t\,\mathbf{RHS}^n$ $\Delta t\,\mathbf{F}(t_n + \frac{8}{15}\Delta t) = -\frac{8}{15}\Delta t\,\mathbf{RHS}^n + \left[Y_b(t_n + \frac{8}{15}\Delta t) - Y^n\right]$ $Y^{''} = Y^{''} + \Delta t\,\mathbf{F}(t_n + \frac{8}{15}\Delta t)$
3	$t_n + \frac{2}{3}\Delta t$	$Y^{iv} = Y^{'} + \frac{5}{12}\Delta t\,\mathbf{RHS}^{''}$ $\Delta t\,\mathbf{F}(t_n + \frac{2}{3}\Delta t) = -\frac{5}{12}\Delta t\,\mathbf{RHS}^{''} + \left[Y_b(t_n + \frac{2}{3}\Delta t) - Y^{'}\right]$ $Y^{iv} = Y^{iv} + \Delta t\,\mathbf{F}(t_n + \frac{2}{3}\Delta t)$
4	$t_n + \Delta t$	$Y^{n+1} = Y^{'} + \frac{3}{4}\Delta t\,\mathbf{RHS}^{iv}$ $\Delta t\,\mathbf{F}(t_n + \Delta t) = -\frac{3}{4}\Delta t\,\mathbf{RHS}^{iv} + \left[Y_b(t_n + \Delta t) - Y^{'}\right]$ $Y^{n+1} = Y^{n+1} + \Delta t\,\mathbf{F}(t_n + \Delta t)$

Table 2.1.: Intermediate steps for low-storage forth-order Runge Kutta method when the body-force method is applied. Time advancement from t_n to $t_{n+1} = t_n + \Delta t$. The RHS term is evaluated using the conservative variables: $RHS^* = RHS(Y^*)$.

The numerical algorithm is summarized in Table 2.1. Some remarks on the implementation of the method are in order:

- The implementation of the method in fully explicit solvers is straightforward. Nevertheless, as shown in table 2.1 for the Runge-Kutta method, the algorithm depends on the time-integration method. The main computational features of the original code (vectorization or parallel solver) are not affected by the method and the additional computational time is negligible.

- The forcing term introduces discontinuities at the interface between the simulated flow and the immersed bodies. When high order methods are used for the spatial discretization, this could trigger unrealistic spatial oscillations (see also Saiki and Biringen, 1996). This is the case of the NTMIX code using sixth order compact finite differences schemes (see also chapter 5 for the description of compact schemes). The most natural way to remove these short-wavelength oscillations was to apply a compact low-pass filter. The sixth-order compact filter (Lele, 1992) was chosen for its lower value of the cut-off wavenumber (only 2% of the flow energy is removed by the filter).

- There exists a flow inside the immersed bodies, which, of course, is not realistic, but it can destabilize the numerical scheme. Interpolation procedures to avoid this phenomenon are necessary at the flow-body interfaces.

2.1.1. Simulation of the tumbling vortex motion

The first application of the implemented body-force method was the simulation of the flow developing in a squared piston compression machine used at IMFT (Institut de Mécanique des Fluides de Toulouse) to study the tumbling vortex motion (Maurel et al., 2001). This typical motion is generated during the intake phase in combustion chambers of spark ignition engines and is characterized by a large scale rotational flow, with the rotation axis perpendicular to the cylinder axis. The large tumbling vortex breaks-up during the compression phase, generating turbulent small scales. Figure 2.2 shows the computational 2D configuration, with a virtual piston moving vertically following a trigonometric law. The original boundary conditions using characteristics analysis of the 1D linearized Navier-Stokes equations (NSCBC method of Poinsot and Lele, 1992) were modified in order to model inflow and outflow conditions through the same boundary. The temporal evolution of the tumbling flow is illustrated by instantaneous velocity field in the animation 2.3.

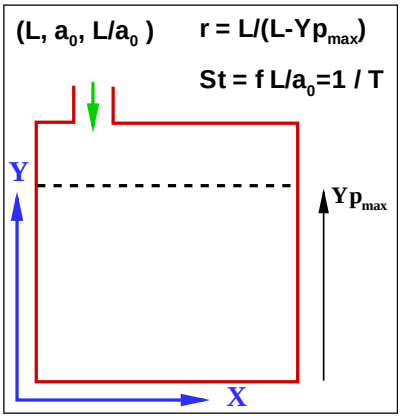

Figure 2.2.: 2D sketch of the squared piston compression machine.

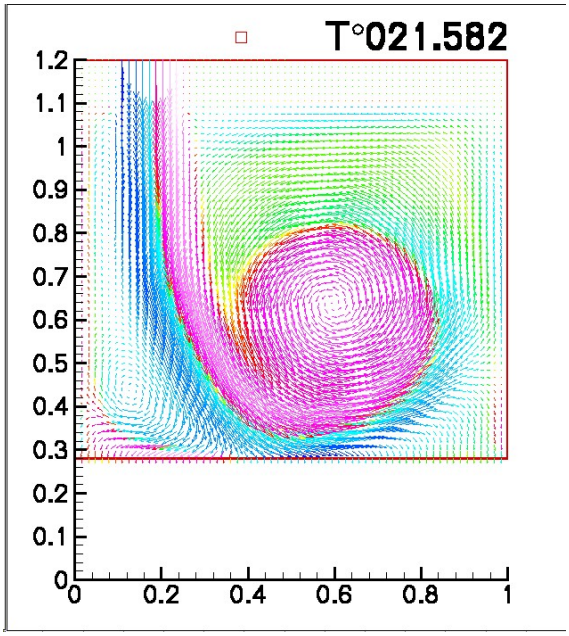

Figure 2.3.: (Animation) Time evolution of velocity vectors during an admission-compression cycle (simulation using an immersed body method).

The method was easily extended to simulate the equivalent three-dimensional configuration. The observed tumbling motion was different, showing the break-up of the tumbling vortex in small vortices, as reported in experimental studies. More details on these simulations are included in an IFP internal report (Danaila, 2001).

2.1.2. Vortex dipoles interacting with obstacles

I have also used the immersed body method to simulate a more academic flow resulting from the interaction of a vortex dipole with obstacles of different shapes. A vortex dipole consists of a pair of opposite-sign vortices, which move together by self induction. Such couples of vortices are encountered in many areas of practical interest (meteorological and coastal flows, trailing vortices from aircrafts, swirled injection in stratified charge engines). Since the interaction of vortex dipoles with walls is an interesting and severe validation test for numerical solvers, I present in the following the analytical formulae that can be used to set, by example, a numerical initial condition.

The structure of a vortex dipole can be analytically described by the Lamb-Chaplygin model (Lamb, 1932), which corresponds to a steady solution of the two-dimensional Euler equations. The vorticity ω is concentrated in a circle of radius a and vanishes outside. The corresponding stream-function for a dipole moving along the negative y-axis is written in polar coordinates (r, θ) under the form:

$$\psi_{in} = CJ_1(kr)\cos\theta, \quad r \leq a,$$

where J_1 is the first order Bessel function and C a constant giving the intensity of the dipole. The exterior flow is considered as irrotational, with constant velocity at infinity equal to the translation velocity (V_c) of the dipole:

$$\psi_{out} = -V_c\left(r - \frac{a^2}{r}\right)\cos\theta, \quad r > a.$$

Matching the two solutions at the circular boundary $r = a$ requires that $J_1(ka) = 0$, with a first zero corresponding to $ka \approx 3.83$. The translation velocity is obtained by imposing the continuity of the tangential velocity $v_\theta = -\partial\psi/\partial r$:

$$V_c = -\frac{C}{2}kJ_1'(ka) \approx -0.771\frac{C}{a}.$$

Note that the radial velocity is also continuous at $r = a$ ($v_r = 1/r\partial\psi/\partial\theta = 0$). The vorticity is finally given by $\omega = -\Delta\psi$:

$$\omega_{in} = k^2\psi_{in}, \quad \omega_{out} = 0.$$

For a numerical simulation, the velocity field to be imposed is finally:

$$v_r = 1/r\partial\psi/\partial\theta, \quad v_\theta = -\partial\psi/\partial r.$$

The animations 2.4 show two examples of vortex dipole interaction with obstacles modeled (gray patches) by the immersed body method. The velocity induced by the vortices generates at the walls thin boundary layers that roll-up to form new dipoles. The complex interaction between different dipoles was carefully investigated in Danaila (2004). This study permitted to document new cases of vortex dipole interactions with walls (for the interaction with infinite walls, see Orlandi and Verzicco, 1993).

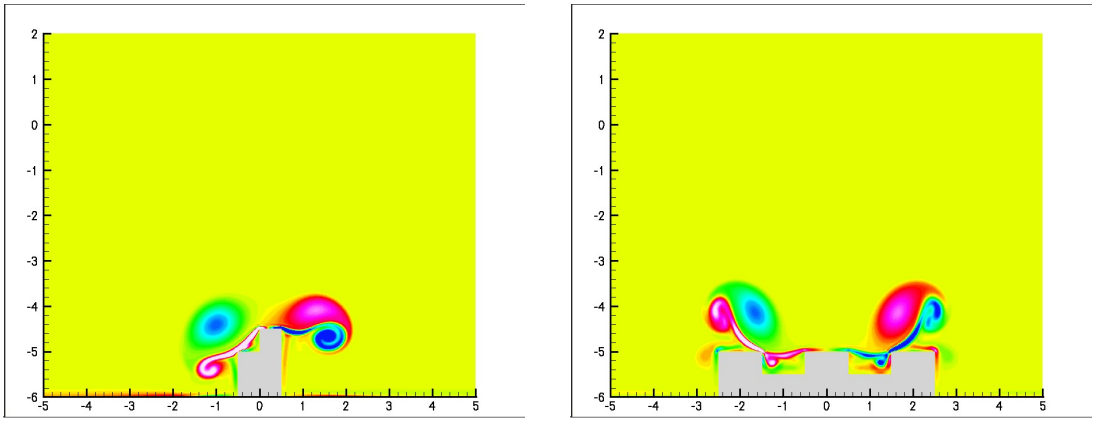

Figure 2.4.: (Animations) Vortex dipole interacting with obstacles modeled (gray patches) with an immersed boundary method. Vorticity field evolution.

2.2. Evaluation of industrial codes and modelling realistic engine injection

The collaborations with IFP also gave me the opportunity to tackle more *industrial* problems, as the evaluation of industrial codes (Danaila and Benteboula, 2004) and the modeling of real injection in internal combustion engines (El Ganaoui et al., 2005). Even thought this research is time consuming and not always considered from an academical point of view, I have the intimate conviction that analyzing real industrial problems could be very useful for a researcher in developing new numerical approaches.

In a technical report (Danaila and Benteboula, 2004) I test the industrial code AVBP on the academic case of the gas-gas injection leading to the formation of a vortex ring. AVBP is a recent example of an academic code (Schönfeld and Rudgyardt, 1999) that became in ten years a largely used industrial code. Initially developed at CERFACS[1], AVBP is nowadays used by a large team including 60 academic and industrial researchers.

[1]Centre Européen de Recherche et de Formation Avancée en Calcul Scientifique, Toulouse.

I was interested in evaluating the behavior of the numerical schemes implemented in AVBP for the resolution of the compressible Navier-Stokes equations. The solver is based on a fully explicit schemes using either a Runge-Kutta or a Lax-Wendroff method. Cell-vertex finite volumes on structured or unstructured meshes are used for the space discretization. Third-order (in space and time) Taylor Galerkin schemes are also available in the code. Characteristics (NSCBC method of Poinsot and Lele, 1992) treatment is used for the boundary conditions. Several subgrid-scale models are available for large eddy simulations (LES) of turbulent flows. The code is announced with impressive performances on MPI parallel computers, with a speed-up of 4078 on 4096 processors (parallel efficiency of 99.5%, http://www.cerfacs.fr/cfd/parallel.php#efficiency). I have installed the code on the Linux cluster of our laboratory, and generally used four processors for the computations.

The considered test case is the gas injection into a quiescent surrounding. The flow is dominated by the vortex ring that rolls-up at the top of the injected jet – this flow will be analyzed in detail in chapter 3. Figure 2.6 shows the propagation of the vortex ring in the cylindrical domain displayed on Fig. 2.5.

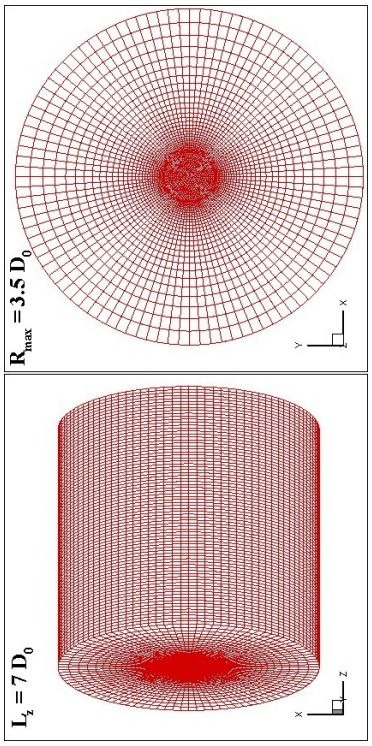

Figure 2.5.: Vortex ring simulation with AVBP: 3D computational domain.

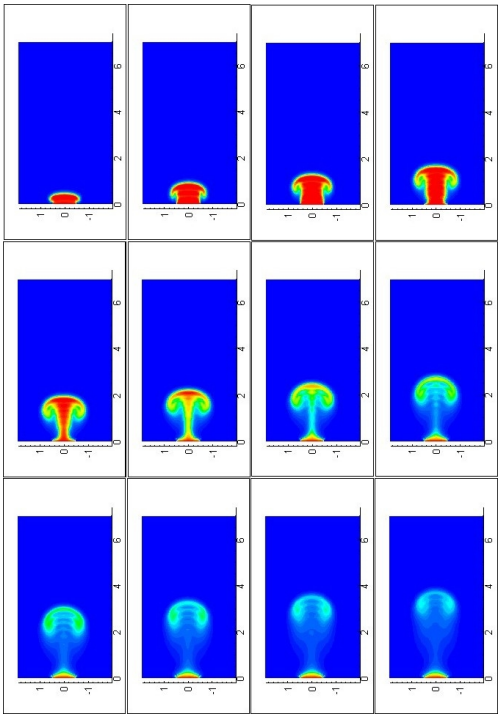

Figure 2.6.: Vortex ring simulation with AVBP: injection of CH_4 in air (2D cuts).

The results obtained using a 3D structured mesh (Fig. 2.5) and the Lax–Wendroff integration method were compared to the results given by my code JETLES (described in chapter 3) that solves incompressible Navier-Stokes equations in cylindrical coordinates. For low injection velocities (Mach number $M = 0.4$), the flow field computed with AVBP is distorted by the presence of pressure (acoustic) waves. However, AVBP accurately predicts important flow quantities, as the vortex ring trajectory and jet penetration length. On the other side, the restrictions on the time step makes this simple 3D computation relatively expensive, even when four or eight processors are used.

In order to reduce the computational (CPU) time, I set up an axisymmetric calculation, which is rarely employed with AVBP. The results are similar to those obtained in the 3D simulation, with an important reduction of the CPU time by a factor of 70. Pressure waves are not visible in the axisymmetric computation if the Mach number of the flow is diminished: for $M < 0.04$ the AVBP and JETLES results are identical for this case.

It is important to mention that this AVBP set-up was also used as a verification tool during the development of the *low-Mach* version of the JETLES code. Preliminary calculations of variable density vortex rings (see section 3.2) were validated against the results generated with AVBP (see Fig. 2.6 for an example of variable density gas-gas injection).

A second part of this applied research activity considered the analysis of real injection conditions, experimentally studied at IFP. This was the main topic of the post-doc research of O. El Ganaoui. An important effort was devoted to the accurate modelling of experimental data in order to provide numerical settings for a numerical simulation of the gas-gas jet generated by a single-hole diesel-like injector. The simulation used the IFP-C3D code, based on Reynolds averaged Navier-Stokes (RANS) equations. Hexahedral finite volume unstructured grids are used for the spatial discretization. The code includes several numerical algorithms like time splitting, the SIMPLE iterative method, explicit subcycle convection. Models like the $k - \varepsilon$ are used for turbulence description and arbitrary Lagrangian Eulerian (ALE) method to compute flows with moving grids.

The numerical results were progressively refined by considering both subsonic and supersonic models for inflow boundary conditions and by evaluating the influence of numerical parameters on the results (mesh sensitivity, numerical dissipation, turbulence model). The final axisymmetric computational set-up (Fig. 2.7) allowed to obtain the best agreement between experimental and numerical jet penetrations, head jet shapes and fuel density profiles (Fig. 2.8). The results are described in El Ganaoui et al. (2005).

It should be noted that the considered case (high pressure direct injection) is not easy to simulate and it represents a severe test case for industrial codes.

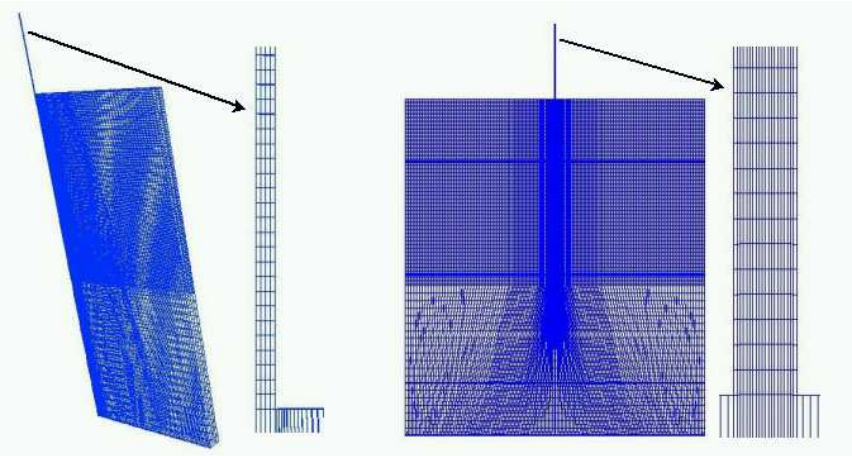

Figure 2.7.: Simulation using the IFP-C3D code (El Ganaoui et al., 2005). Axisymmetric and 2D computational domains.

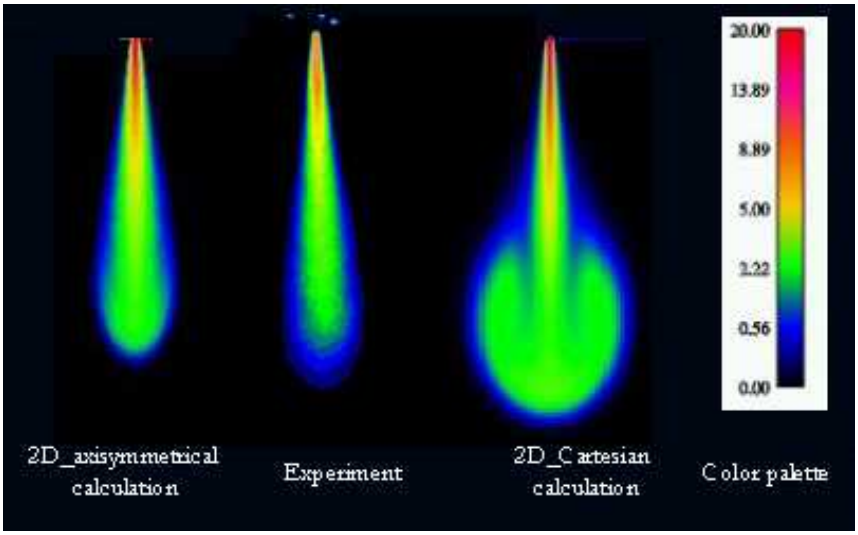

Figure 2.8.: Simulation using the IFP-C3D code (El Ganaoui et al., 2005). Evolution of the fuel jet: comparison between axisymmetric computation, experimental visualization and 2D computation.

3. Finite differences method for the simulation of incompressible fluid flows in cylindrical coordinates: the JETLES code

General presentation

This is the main research activity that I have been developing in the field of numerical simulation of *classical* fluid flows. After my PhD, I have decided to build my own Navier-Stokes code for the simulation of low-speed round jets. I have naturally chosen to develop an incompressible Navier-Stokes solver in cylindrical coordinates. The new code JETLES (JET Large Eddy Simulations) allows numerical simulations of 3D or axisymmetric flows evolving in time and space in cylindrical domains (round jets, vortex rings, etc.). The code uses ideas from the homonymous *temporal* code written by Paolo Orlandi (University of Rome); I acknowledge here his useful input during the initial development of this code. A detailed description of the numerical method for the temporal simulation (*i. e.* with periodic boundary condition in the streamwise direction) is now available in the book of Orlandi (1999).

Finite differences schemes and time-integration methods that are appropriate for the formulation of the equations in cylindrical coordinates were studied and progressively integrated in the code. Important theoretical issues related to this formulation (treatment of the singularity introduced by the axis, boundary conditions, Poisson solver) were also addressed. From the implementation point of view, the code has been optimized to be effective on individual workstations. Using a single processor, the computational time for high resolution simulations is considerably reduced, compared to industrial or commercial codes. Written in Fortran, the code has a simple architecture permitting to be rapidly understood by students with reduced programming experience. The development of the code was also part of the research of my students, M. Ballestra (MSc) and S. Benteboula (PhD).

The JETLES code was used to simulate academic flows related to industrial applications, such as the fuel injection in internal combustion engines. This applicative part was partially supported by the Institut Français du Pétrole (IFP) and, re-

cently, by Continental Automotive France. The code, described in the report [R1], continuously evolves towards new applications presented in the next chapter.

This chapter describes in great detail the numerical method used for the incompressible Navier-Stokes equations in cylindrical coordinates. The extension of the code to deal with low-Mach number flows (PhD of S. Benteboula) is also briefly presented. The main obtained results on the analysis of the vortex ring flow are finally reported.

Key words: finite differences, staggered grids, incompressible Navier-Stokes equations, low-Mach approximation, cylindrical coordinates, round jet, vortex ring.

Publications :

articles	: [A1, A2, A4, A5, A12],
reports	: [R2, R3],
JETLES handbook	: [R1],
numerical codes	: [Code3].

Collaborations : J. Hélie (Continental Automotive France), C. Habchi, C. Angelberger (Institut Français du Pétrole), P. Orlandi (University of Rome), B. J. Boersma (Technical University Delft, The Netherlands), L. Djenidi, R. A. Antonia (University of Newcastle, Australia).

3.1. Numerical resolution of the incompressible Navier-Stokes equations

3.1.1. Navier-Stokes equations in cylindrical coordinates

The incompressible Navier-Stokes equations, written in cylindrical coordinates (r, θ, z) are discretized by a finite differences method described in Orlandi (1999). The singularity introduced by the axis $r = 0$ is avoided by using a formulation in primitive variables $(q_\theta = v_\theta, q_r = v_r \cdot r, q_z = v_z, p)$ and a staggered grid.

Navier-Stokes equations in cylindrical coordinates are:
• the mass conservation equation:

$$\frac{1}{r}\left(\frac{\partial q_\theta}{\partial \theta} + \frac{\partial q_r}{\partial r} + r\frac{\partial q_z}{\partial z}\right) = 0 \tag{3.1.1}$$

• the momentum conservation equations:

$$\begin{aligned}
\frac{Dq_\theta}{Dt} &= -\frac{1}{r}\frac{\partial p}{\partial \theta} + \frac{1}{Re}\left[\frac{1}{r^2}\left(\frac{\partial}{\partial r}r^3\frac{\partial}{\partial r}\frac{q_\theta}{r}\right) + \frac{1}{r^2}\frac{\partial^2 q_\theta}{\partial \theta^2} + \frac{\partial^2 q_\theta}{\partial z^2} + \frac{2}{r^3}\frac{\partial q_r}{\partial \theta}\right] \\
\frac{Dq_r}{Dt} &= -r\frac{\partial p}{\partial r} + \frac{1}{Re}\left[r\frac{\partial}{\partial r}\left(\frac{1}{r}\frac{\partial q_r}{\partial r}\right) + \frac{1}{r^2}\frac{\partial^2 q_r}{\partial \theta^2} + \frac{\partial^2 q_r}{\partial z^2} - \frac{2}{r}\frac{\partial q_\theta}{\partial \theta}\right] \\
\frac{Dq_z}{Dt} &= -\frac{\partial p}{\partial z} + \frac{1}{Re}\left[\frac{1}{r}\frac{\partial}{\partial r}\left(r\frac{\partial q_z}{\partial r}\right) + \frac{1}{r^2}\frac{\partial^2 q_z}{\partial \theta^2} + \frac{\partial^2 q_z}{\partial z^2}\right]
\end{aligned} \tag{3.1.2}$$

with substantial derivatives:

$$\begin{aligned}
\frac{Dq_\theta}{Dt} &= \frac{\partial q_\theta}{\partial t} + \frac{1}{r^2}\frac{\partial}{\partial r}\left(r q_r q_\theta\right) + \frac{1}{r}\frac{\partial}{\partial \theta}\left(q_\theta q_\theta\right) + \frac{\partial}{\partial z}\left(q_\theta q_z\right) \\
\frac{Dq_r}{Dt} &= \frac{\partial q_r}{\partial t} + \frac{\partial}{\partial r}\left(\frac{q_r q_r}{r}\right) + \frac{\partial}{\partial \theta}\left(\frac{q_r q_\theta}{r}\right) + \frac{\partial}{\partial z}\left(q_r q_z\right) - q_\theta q_\theta \\
\frac{Dq_z}{Dt} &= \frac{\partial q_z}{\partial t} + \frac{1}{r}\frac{\partial}{\partial r}\left(q_r q_z\right) + \frac{1}{r}\frac{\partial}{\partial \theta}\left(q_\theta q_z\right) + \frac{\partial}{\partial z}\left(q_z q_z\right)
\end{aligned} \tag{3.1.3}$$

The Reynolds number is a dimensionless parameter of the flow, defined as $Re = VL/\nu$, where ν is the kinematic viscosity of the flow, V a characteristic velocity scale and L a length scale of the flow.

3.1.2. Time integration by a fractional step method

Momentum equations are advanced in time using a fractional-step method (Kim and Moin, 1985), based on a combination of a low-storage third-order Runge–Kutta scheme for the convective terms and a semi-implict Crank–Nicolson scheme for the viscous terms. For each substep of the integration scheme, a Poisson pressure correction equation is solved to satisfy the continuity equation.

More in detail, the equations (3.1.1) and (3.1.2) are solved by a projection method, also called *fractional step method*. This method was proposed by Rai and Moin (1991) and modified by Verzicco and Orlandi (1996). The time integration is based on a three-steps Runge–Kutta method: for each substep $l = 1, 2, 3$:

(A) a non-solenoidal velocity field ($\widehat{q}^l$) is computed from the momentum equations with an explicit treatment of convective and pressure gradient terms and semi-implicit treatment (Crank–Nicolson scheme) of viscous terms: the discretized equations are written in the compact form as:

$$\frac{\widehat{q}_c^l - q_c^l}{\Delta t} = \left[\gamma_l \mathcal{H}_c^l + \rho_l \mathcal{H}_c^{l-1} - \alpha_l \mathcal{G}_c p^l + \frac{\alpha_l}{2}\mathcal{A}_c\left(\widehat{q}_c^l + q_c^l\right)\right], \quad \text{pour} \quad c = \theta, r, z, \tag{3.1.4}$$

where $\mathcal{H}$ contains explicit terms (convective and cross-derivatives viscous terms) and $\mathcal{A}$ the remaining viscous terms.

The time integration coefficients are analytically derived in order to obtain a second order accuracy in time. Rai and Moin (1991) obtained the values for $(\alpha_l, \gamma_l, \rho_l)$ for a 3-step second order scheme. In Danaila (1999–2008), I derive a family of Runge–Kutta methods for which the second order is obtained in two steps only. These latter schemes bring an important computational time reduction. Note that it is important to impose in these integration schemes that $\rho_1 = 0$ in order to make the method self starting.

The discretized equations (3.1.4) are solved by an approximate factorization procedure (ADI). The resulting tridiagonal linear systems are solved by an optimized LU method.

(B) the field ($\widehat{q}^l$) is corrected to satisfy the continuity equation (3.1.1).

The correction equation:

$$q_c^{l+1} - \widehat{q}_c^l = -\alpha_l \, \Delta t \, \mathcal{G}_c \Phi^{l+1}, \qquad c = \theta, r, z, \tag{3.1.5}$$

leads to a Poisson equation if substituted in the continuity equation:

$$\mathcal{L}\Phi^{l+1} = \frac{1}{\alpha_l \Delta t}\, \mathcal{D}\vec{\widehat{q}}^{\,l}. \tag{3.1.6}$$

The gradient, divergence and Laplacian operators are defined in the classical way by:

$$\mathcal{G} = \left(\frac{1}{r}\frac{\partial}{\partial\theta}, r\frac{\partial}{\partial r}, \frac{\partial}{\partial z} \right),$$

$$\mathcal{D} = \frac{1}{r}\frac{\partial}{\partial\theta} + \frac{1}{r}\frac{\partial}{\partial r} + \frac{\partial}{\partial z},$$

$$\mathcal{L} = \mathcal{D}\mathcal{G} = \frac{1}{r^2}\frac{\partial^2}{\partial\theta^2} + \frac{1}{r}\frac{\partial}{\partial r}\left(r\frac{\partial}{\partial r} \right) + \frac{\partial^2}{\partial z^2}.$$

It is important to note that the boundary conditions needed in (3.1.6) have to be compatible, via the correction equation (3.1.5), with the boundary conditions imposed to the non-solenoidal field.

The Poisson equation (3.1.6) is solved using a FFT (Fast Fourier Transform) in the (naturally periodic) azimuthal direction θ and a cyclic reduction algorithm for the remaining two-dimensional system. The last step is implemented via a subroutine from the **FISHPACK** Fortran library (for details, see Ballestra, 2002).

(C) Once the scalar field Φ computed, the correction equation (3.1.5) is used to calculate the solenoidal field q_c^{l+1}, with $c = \theta, r, z$. The pressure gradient is finally updated by:

$$\mathcal{G}_c p^{l+1} = \mathcal{G}_c p^l + \mathcal{G}_c \Phi^{l+1} - \frac{\alpha_l \, \Delta t}{2} \mathcal{A}_c \left(\mathcal{G}_c \Phi^{l+1} \right). \tag{3.1.7}$$

The steps (A)-(B)-(C) are repeated for each substep of the Runge–Kutta method.

3.1.3. Space discretization: finite differences on staggered grids

The computational domain is cylindrical (Fig. 3.1), defined by its maximum length (L_z) and radius R_{max}. The grid points are distributed uniformly in the azimuthal (θ) and axial (z) directions; the uniform grid in θ direction is required by the use of a FFT in the Poisson solver. In the radial direction r, the grid is stretched using different coordinate transformations based on hyperbolic tangent functions (for details, see Ballestra, 2002).

Spatial derivatives are approximated by centered finite differences schemes on a staggered grid. Velocity fluxes are defined on the cell surfaces (see Fig. 3.1) while the pressure p and the variable Φ, related to it, are defined at the cell centers. At $r = 0$, only q_r is defined, and since by definition $q_r = 0$ at this location, no ad-hoc boundary conditions are required at $r = 0$. For the stretched grid in the radial

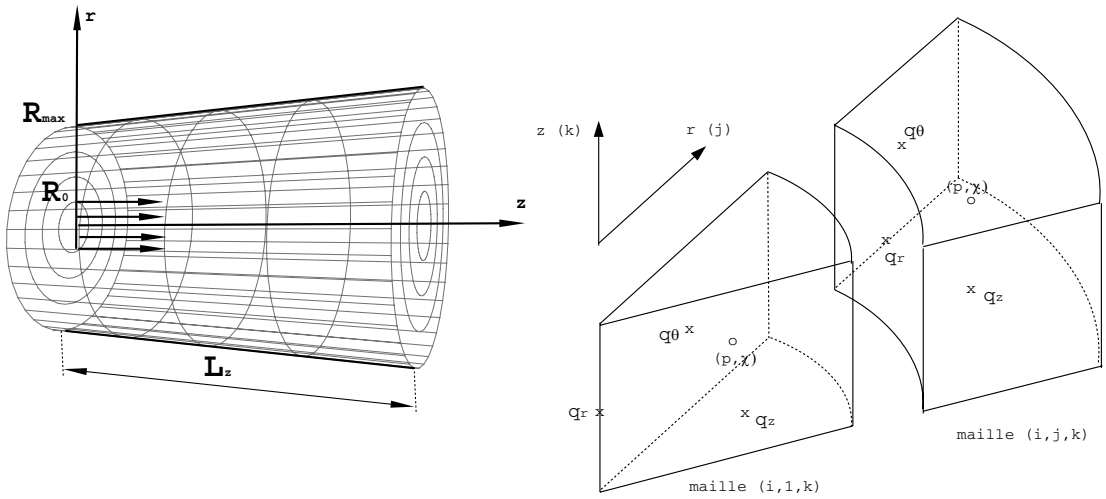

Figure 3.1.: Computational domain and staggered grids.

direction, we have studied (Ballestra, 2002) different approximations schemes for the derivatives: the best approximation is given by a numerical evaluation of the metrics instead of their analytical expressions.

The boundary conditions are adapted to each computational case and recalled in section 3.3 presenting numerical results. Several issues on the behaviour of different boundary conditions are discussed in Danaila (1999–2008) and Benteboula (2006).

3.2. Numerical resolution of low-Mach number Navier-Stokes equations

An existing Navier-Stokes solver for incompressible (constant density) flows can be easily extended to deal with variable density flows by implementing a low-Mach number approximation. The Mach number M is defined as the ratio V/a, where V is the characteristic velocity scale of the flow and a the sound velocity. The Navier-Stokes equations in the low-Mach approximation keep similar forms as the incompressible equations, with a supplementary evolution equation for the density (or temperature). From a practical point of view, this is a considerable advantage since the projection method described in the previous section can be used. In particular, the Poisson solver, which is a major part of a numerical code, remains exactly the same.

Another advantage of the low-Mach formulation is the possibility to simulate variable density flows for low speeds. As we have already seen in section 2.2 of this

report, using compressible Navier-Stokes solvers to simulate such flows results in important restrictions on the time step, imposed by the existence of pressure waves in the flow. The time step goes theoretically to zero when $M \to 0$. The low-Mach formulation removes this restriction, but is valid only for flows with density variations due exclusively to temperature gradients. Hopefully, such flows are encountered in many areas of practical interest (oceanic flows, combustion, reacting flows with heat release, etc.)

Mathematical theories of low-Mach number flows are used in an attempt to prove the convergence of the compressible formulation to the incompressible one when the Mach number tends to zero. A review of such mathematical theories is given in the *Special issue on low Mach number flows*, M2AN, Vol. 39, 2005. From the numerical implementation point of view, several formulations are used in the literature (see, for instance, Knio et al., 2000; Majda and Sethian, 1985; Cook and Riley, 1996), depending on the flow and the numerical scheme.

The low-Mach formulation implemented in cylindrical coordinates in the JETLES code is described in great detail in the PhD Thesis of my student S. Benteboula. I give in the following only the main ideas for deriving the governing equations and for building a low-Mach Navier-Stokes solver. The results on the evolution of a variable density vortex ring are presented in the next section (3.3) of this chapter.

3.2.1. Low-Mach number approximation

The low-Mach formulation is obtained from the compressible Navier-Stokes equation by introducing a power series expansion of primitive variables. The small parameter will obviously depend on the Mach number M. We have used a methodology with a single pressure scale that eliminates the acoustic waves from the flow field. The small parameter in this case is chosen as $\epsilon = \gamma M^2$. The power series expansions of the density ρ, velocity $\mathbf{v}$, pressure p et volume energy e become:

$$\rho = \rho_0 + \epsilon\rho_1 + \mathcal{O}(\epsilon^2), \tag{3.2.1}$$
$$\mathbf{v} = \mathbf{v}_0 + \epsilon\mathbf{v}_1 + \mathcal{O}(\epsilon^2), \tag{3.2.2}$$
$$T = T_0 + \epsilon T_1 + \mathcal{O}(\epsilon^2), \tag{3.2.3}$$
$$p = p_0 + \epsilon p_1 + \mathcal{O}(\epsilon^2), \tag{3.2.4}$$

$$\rho e = \frac{p_0}{\gamma - 1} + \epsilon\frac{p_1}{\gamma - 1} + \epsilon\rho_0\frac{{\mathbf{v}_0}^2}{2} + \mathcal{O}(\epsilon^2). \tag{3.2.5}$$

Substituting these expansions in the dimensionless compressible Navier-Stokes equations (see, for example, the equation 2.1.1) and after separation of terms of the same order, several simplifications are obtained. The first comes from the momentum

equation and states that the hydrodynamic pressure p_0 does not depend on spatial variables ($\nabla p_0 = 0$). If open flows are considered, as in our case, it is reasonable to suppose that p_0 is constant in time also. In other terms, the fluctuations of the dynamical pressure p_1 are negligible compared to the value of p_0. A second simplification is obtained for the energy equation, which can be combined to the mass conservation equation to get (see also Cook and Riley, 1996) an evolution equation for the density ρ:

$$\frac{\partial \rho_0}{\partial t} = -\mathbf{v}_0 \cdot \nabla \rho_0 - \frac{1}{T_0}\left[\frac{1}{RePr}\nabla \cdot (\mu \nabla T_0)\right], \quad \text{with the state law} \quad p_0 = \rho_0 T_0. \tag{3.2.6}$$

The momentum equations have the same form as the incompressible equations:

$$\frac{\partial \rho_0 \mathbf{v}_0}{\partial t} + \nabla \cdot (\rho_0 \ \mathbf{v}_0 \otimes \mathbf{v}_0) = -\nabla p_1 + \frac{1}{Re}\nabla \cdot \vec{\vec{\tau}}_0, \tag{3.2.7}$$

$$\tau_0 = -\frac{2}{3}\mu(\nabla \mathbf{v}_0) \cdot \vec{\vec{I}} + \mu(\nabla \mathbf{v}_0 + \nabla^t \mathbf{v}_0),$$

which suggests to use the same numerical algorithms to solve these equations. The only technical difficulty is introduced by the fact that the viscosity (μ) is now variable, depending on the temperature T following the Sutherland law: $\mu = T^b$, with $b = 0.75$. This means that the coefficients of the matrices of the linear systems have to be updated at each time step, resulting in an increase of the computational time.

The lengthy form of the final equations written in cylindrical coordinates is presented in Benteboula (2006) and will not be given here. I summarize in exchange, some ideas on the numerical algorithm developed for the implementation of the low-Mach approximation:

• The cylindrical computational domain and the staggered grid (Fig. 3.1) remain unchanged; the new variable ρ is computed at cell centers.

• The evolution of the density is governed by the convection-diffusion equation (3.2.6). Since large density gradients have to be captured by the numerical scheme without introducing oscillations, we have used a TVD (*Total Variation Diminishing*) scheme.

The TVD scheme developed by Vreugenhil and Koren (1993) for computing combustion flows allows to keep the density value inside the prescribed range (usually $0 < \rho \leq 1$). The general form of the scheme, applied for the treatment of convective terms, is:

$$\frac{\partial}{\partial x}(\rho v) = \frac{\mathcal{F}_{i+\frac{1}{2}} - \mathcal{F}_{i-\frac{1}{2}}}{\delta x}, \tag{3.2.8}$$

where

- for $v_{i+\frac{1}{2}} > 0$ the flux at the interface $i + \frac{1}{2}$ is computed as:

$$\begin{cases} \mathcal{F}_{i+\frac{1}{2}} = \left[\rho_i + \dfrac{1}{2}\Phi(c_{i+\frac{1}{2}})(\rho_i - \rho_{i-1})\right] v_{i+\frac{1}{2}}, \\ c_{i+\frac{1}{2}} = \dfrac{\rho_{i+1} - \rho_i + \varepsilon}{\rho_i - \rho_{i-1} + \varepsilon}, \end{cases} \tag{3.2.9}$$

- while for $v_{i+\frac{1}{2}} < 0$ the same flux becomes:

$$\begin{cases} \mathcal{F}_{i+\frac{1}{2}} = \left[\rho_{i+1} + \dfrac{1}{2}\Phi(c_{i+\frac{1}{2}})(\rho_{i+1} - \rho_{i+2})\right] v_{i+\frac{1}{2}}, \\ c_{i+\frac{1}{2}} = \dfrac{\rho_i - \rho_{i+1} + \varepsilon}{\rho_{i+1} - \rho_{i+2} + \varepsilon}, \end{cases} \tag{3.2.10}$$

  with $\varepsilon = 10^{-11}$ and the limiter

$$\Phi(c) = \max\left[0, \min\left(2c, \min\left(\frac{1}{3} + \frac{2}{3}c + 2\right)\right)\right]. \tag{3.2.11}$$

• For the time integration of the momentum equations (3.2.7) the same projection method as for the incompressible equations can be used. The Poisson correction equation has now a supplementary source term:

$$\mathcal{L}\Phi^{l+1} = \frac{1}{\alpha_l \Delta t}\left[\mathcal{D}\vec{\widehat{q}}^{\,l} + \left(\frac{\partial \rho}{\partial t}\right)^{n+1}\right], \tag{3.2.12}$$

but the elliptic solver remains strictly the same (FFT+cyclic reduction), which is a real advantage for the implementation.

• Several numerical schemes have been studied in Benteboula (2006):
1- A fully explicit Adams-Bashforth scheme (second order in time).
2- A predictor-corrector Adams-Bashforth/Adams-Moulton scheme (second order in time).
3- An explicit (first order) Euler scheme for the density equation and a semi-implicit (second order) Adams-Bashforth/Crank-Nicolson scheme for the momentum equations.
4- An explicit (first order) Euler scheme for the density equation and an explicit (second order) Adams-Bashforth scheme for the momentum equations.
Intensive numerical tests showed that the fourth scheme displays the best stability characteristics and the lowest computational time for the same overall convergence rate. This scheme was proved effective in simulating flow with very large density gradients; some examples from Benteboula (2006) are presented in the next section.

3.3. Numerical simulation of the vortex ring flow

3.3.1. Vortex rings

The fundamental and practical interest of the scientific community in vortex rings has generated a large volume of literature for at least a hundred years. Theoretical analysis of this flow can be found in classical textbooks (e. g. Saffman, 1992; Batchelor, 1988) or several review papers (Shariff and Leonard, 1992). The compact toroidal structure of vortex rings is encountered in many real flows. The most common is the smoke ring that skilled smokers are able to form by controlling the flow at their lips. Vortex rings also appear when the blood enters the left ventricle of the heart, during volcano eruptions (Fig. 3.2), in the wake of flying of swimming animals, etc.

I was interested in such flows because of more practical reasons, related to the presence of vortex rings in the flow developing in internal combustion engines during the injection phase (see also chapter 2). The fuel charge in direct-injection spark-ignition internal combustion engine is directly injected in the combustion chamber by an injector delivering a jet of fuel droplets (or spray) (see Fig. 3.3). An axisymmetric vortex forms at the top of the spray and dominates the flow determining the main characteristics of the flow (as the penetration length) important for engine design. The purpose of this processus is to generate an enhanced mixing in the vicinity of the spark plug. Industrial codes have to deal with a lot of parameters of the real in-cylinder flow and generally under-predicts the penetration length of the spray. This is illustrated in Fig. 3.3 showing a calculation with the *KIVA-MB* code, compared to experimental data.

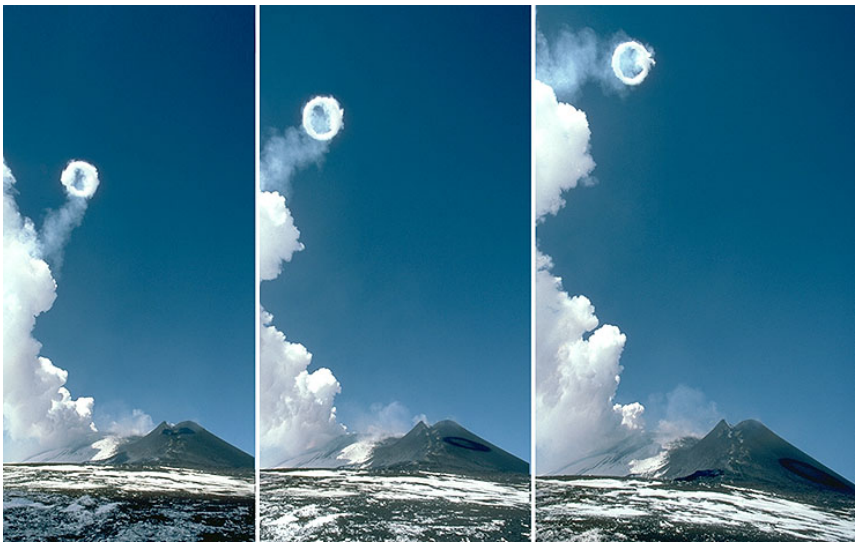

Figure 3.2.: Smoke vortex ring formed during the eruption of Etna volcano (http://www.stromboli.net).

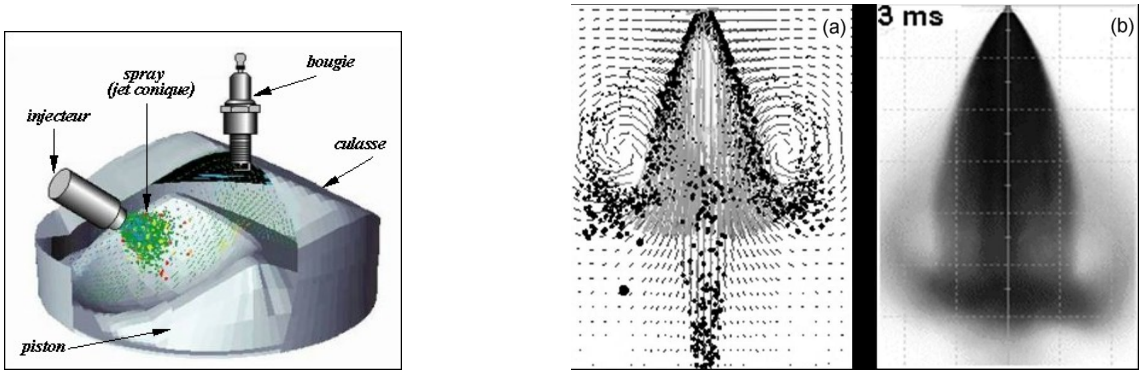

Figure 3.3.: Sketch of a direct-injection spark-ignition combustion engine. (a) Simulation of a two-phase flow (spray) with the *KIVA-MB* code (b) Corresponding experience performed at IFP. From Ballestra (2002).

3.3.2. Evolution of the constant density vortex ring

Laminar vortex rings are usually generated in laboratory by a piston/cylinder arrangement sketched in Fig. 3.4. A column of fluid is pushed by a piston into a quiescent surrounding. The flow is visualized by injecting a passive marker (dye in water and smoke in air). The boundary layer at the edge of the cylinder separates and rolls-up into a vortex ring. This is the formation phase of the vortex ring.

After the piston stops, the vortex ring continues to entrain surrounding irrotational fluid and a part of its wake. At later times, a vortex bubble is formed, also called vortex atmosphere. Inside the vortex atmosphere, the fluid circulates over closed

streamlines. The vortex ring has the shape of an oblate ellipsoid of revolution, with the vorticity concentrated in the vortex core $\partial\Omega_c$. This is the postformation phase.

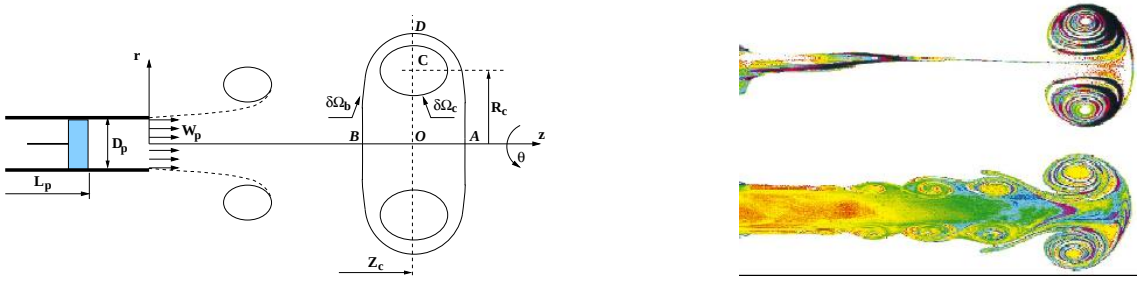

Figure 3.4.: Sketch of the formation and postformation phases of a vortex ring. Experimental visualizations by Gharib et al. (1998).

For long duration injections, Kelvin–Helmholtz instabilities develop in the wake of the vortex ring, as displayed in Fig. 3.4. The animation 3.5 shows complex vortex interactions in an annular jet flow submitted to controlled perturbations at the nozzle.

In a recent paper (Danaila and Hélie, 2008) we study the postformation evolution of a laminar vortex ring by means of high resolution axisymmetric simulations (301×1251 grid points). The vortex topology is described by calculating the embedded domains of the vortex inner core, vortex core and vortex bubble. The structure of the vortex ring is found to be self-similar during the entire postformation phase. Numerical simulations also allowed to correct the apparent discrepancy between different experimental (Dabiri and Gharib, 2004) and theoretical studies reporting power-laws for the mathematical description of the evolution of translation velocity and integrals of motion (circulation, impulse and energy).

The practical interest of these computations was to evaluate if ideal vortex models are pertinent in describing realistic vortex rings. The computationally generated vortex rings are matched to the classical Norbury–Fraenkel model and the recent model proposed by Kaplanski and Rudi. It is proved that these models offer a good prediction of integral quantities, and a relatively accurate description of the vortex ring topology (see Fig. 3.6). In exchange, both models underestimate the volume of fluid carried inside the vortex bubble.

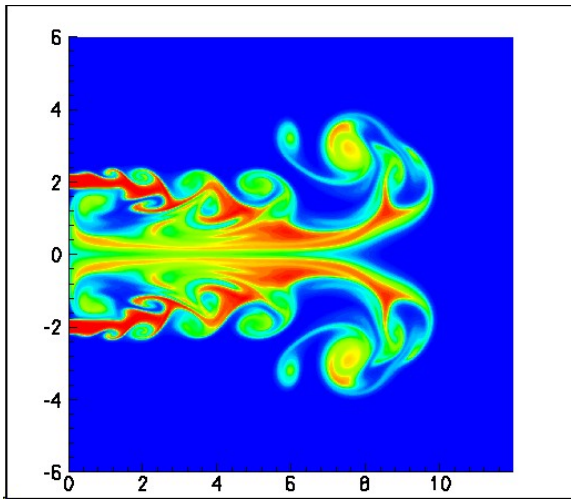

Figure 3.5.: (Animation) Vortex roll-up and vortex interactions in an annular jet for a long time injection. Evolution of the passive scalar in an axisymmetric simulation.

It could be interesting to recall here the ideal vortex model derived by Kaplanski and Rudi (2005). Their viscous vortex ring model displays more realistic characteristics, when computing the vortex topology or the vortex signature (Moffatt, 1988). A vortex from this family is identified by the ratio $\tau = R_c/\ell$, where R_c is the radius of the vortex and ℓ a viscous scale. The vorticity distribution is Gaussian:

$$\omega = \Omega \exp\left(-\frac{1}{2}\left(\sigma^2+\eta^2+\tau^2\right)\right)\mathbf{I_1}(\sigma\tau), \tag{3.3.1}$$

with $\sigma = r/\ell, \eta = (z - Z_c(t))/\ell$ and Z_c the axial coordinate of the vortex center. Analytical expressions for the circulation Γ, energy E and translation velocity W are derived from Navier-Stokes by analytical developments using modified Bessel functions ($\mathbf{I}$) and generalized hypergeometric functions (${}_2F_2$):

$$\Gamma = \Gamma_0\left(1-\exp\left(-\frac{\tau^2}{2}\right)\right), \quad \Gamma_0 = \frac{I}{\pi R_c^2}, \tag{3.3.2}$$

$$E = \frac{I^2}{2\pi^2}\frac{\tau}{R_c^3}\left(\frac{1}{12}\sqrt{\pi}\tau^2\,{}_2F_2\left(\left\{\frac{3}{2},\frac{3}{2}\right\},\left\{\frac{5}{2},3\right\},-\tau^2\right)\right), \tag{3.3.3}$$

$$\begin{aligned} W = \frac{I}{4\pi^2}\frac{\tau}{R_c^3} \quad & \left\{3\sqrt{\pi}\exp\left(-\frac{\tau^2}{2}\right)\mathbf{I}_1\left(\frac{\tau^2}{2}\right)\right. \\ & +\frac{1}{12}\sqrt{\pi}\tau^2\,{}_2F_2\left(\left\{\frac{3}{2},\frac{3}{2}\right\},\left\{\frac{5}{2},3\right\},-\tau^2\right) \\ & \left.-\frac{3}{5}\sqrt{\pi}\tau^2\,{}_2F_2\left(\left\{\frac{3}{2},\frac{5}{2}\right\},\left\{2,\frac{7}{2}\right\},-\tau^2\right)\right\}. \end{aligned} \tag{3.3.4}$$

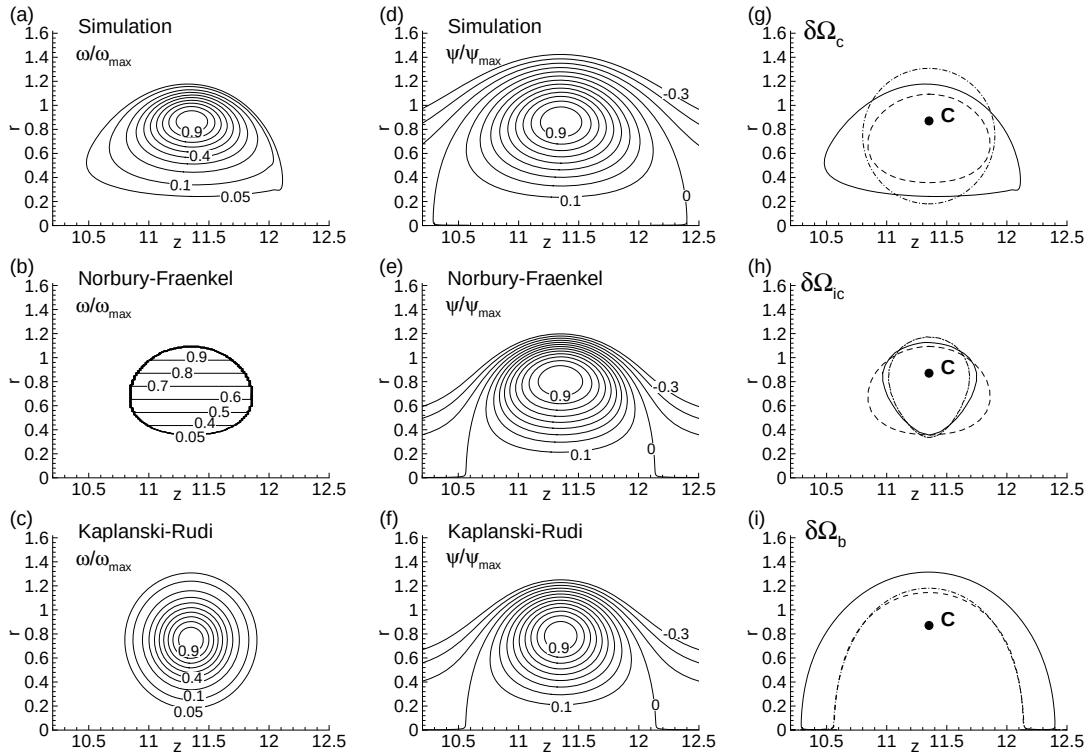

Figure 3.6.: Constant density vortex ring. Comparison between numerical results and ideal vortex ring models. Iso-contours of vorticity (ω), stream function (ψ) and contours of embedded domains defining the vortex topology. From Danaila and Hélie (2008).

3.3.3. Evolution of the variable density vortex ring

The structure of the vortex ring changes when the injected flow has different temperature from the surrounding (Fig. 3.7). Simulations with the low-Mach number version of the JETLES code used as parameter the ratio $\alpha = T_j/T_a = \rho_a/\rho_j$ between the jet temperature T_j and ambiance temperature T_a. A large range of values ($\alpha \in [1/10, 10]$) was explored in the PhD of Benteboula (2006), with a large variety of vortex topologies reported. The new vortex dynamics is found to be strongly influenced by the baroclinic torque.

From a practical point of view, the temperature ratio α affects the quantities of interest for the engine design: penetration length, vortex circulation, decay of the fuel concentration along the axis, etc. Figure 3.8 shows a quasi-linear time variation of the penetration length, with greater slopes for the cold injection. This results was

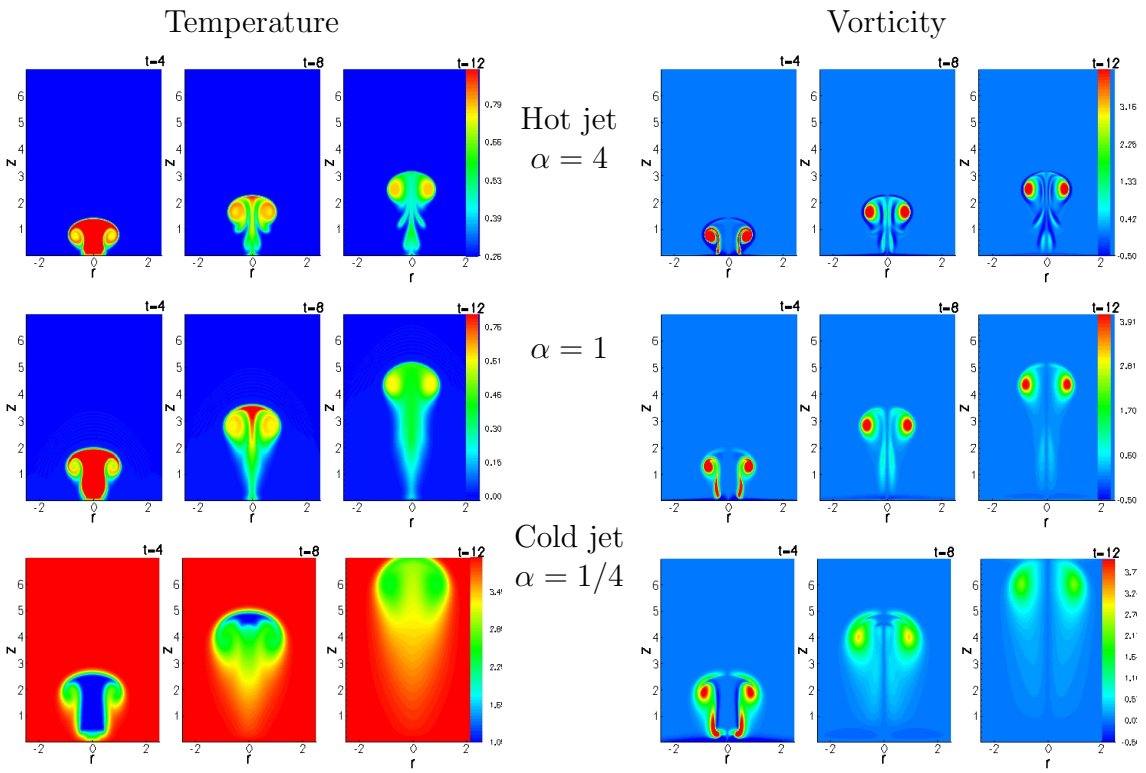

Figure 3.7.: Vorticity and temperature maps for different cases of variable density vortex rings. From Benteboula (2006).

expected, since the cold jet is heavier and propagates faster in a lighter ambiance. A related phenomenon is the decrease with α of the propagation velocity of the jet. The flow circulation is also affected: colder is the jet, bigger is the maximum circulation, as illustrated in Fig. 3.8. This phenomenon was explained by the fact that for a hot jet, the baroclinic torque is opposed to the roll-up of the vortex ring.

As a last remark, I should emphasize the fact that,when starting this activity, theoretical or numerical results on variable vortex rings were not available in the literature. This was the reason why the first simulations were validated by running other similar numerical codes. The low-Mach version of the spherical coordinates code provided by B. J. Boersma (code also presented in section 1.2) was used for this purpose. The results on the evolution of variable density vortex rings are presented in Benteboula (2006); Benteboula and Danaila (2007); Danaila and Benteboula (2004); Benteboula and Danaila (2006).

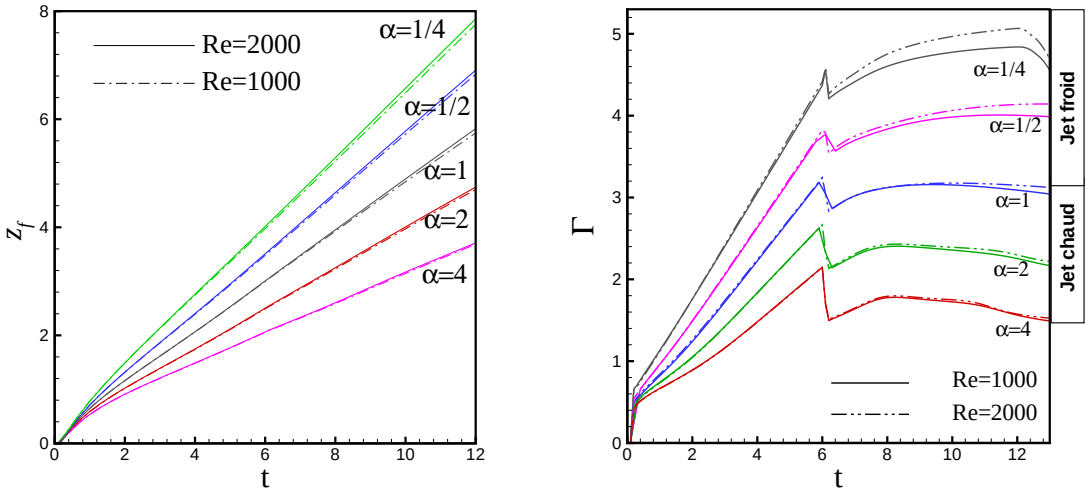

Figure 3.8.: Time evolution of the penetration length Z_f and circulation Γ for different cases of variable density injection. From Benteboula (2006).

4. Work in progress and future plans

Future work on the numerical simulation of classical fluids will follow three main directions:

- numerical and theoretical analysis of ideal vortex models,
- numerical simulations and modeling of the injection velocity profile by studying the flow in the entry region of a pipe,
- further development of the JETLES code for the simulation of conical injection flows that are used in recent internal combustion engines.

4.1. Numerical and theoretical analysis of vortex models

In Danaila and Hélie (2008), we have compared numerical data with the description of vortex rings by ideal vortex models. The commonly used vortex ring model is the Norbury–Fraenkel model, based on a numerical study by Norbury (1973). Only tabulated data are available to describe vortex topology, which makes the use of this model cumbersome. Besides, the used numerical algorithms are not well documented and their convergence is not proved. Consequently, I have started to revisit the numerical work on ideal vortex models.

The mathematical theory of steady, non viscous, vortex ring models considers the following elliptical nonlinear partial differential equation:

$$\mathcal{L}\psi = \frac{\partial^2\psi}{\partial z^2} + r\frac{\partial}{\partial r}\left(\frac{1}{r}\frac{\partial\psi}{\partial r}\right) = \begin{cases} -r^2 f(\psi), & \text{in} \quad \Omega_c \\ 0, & \text{in} \quad \Pi\backslash\bar{\Omega}_c, \end{cases} \tag{4.1.1}$$

where $\Pi = \{(z,r)|r>0\}$. The unknown function ψ is the Stokes stream function of the flow and Ω_c is the domain defining the vortex core (Fig. 4.1). Ω_c is the domain where the vorticity, represented by the function $f(\psi)$, is non zero.

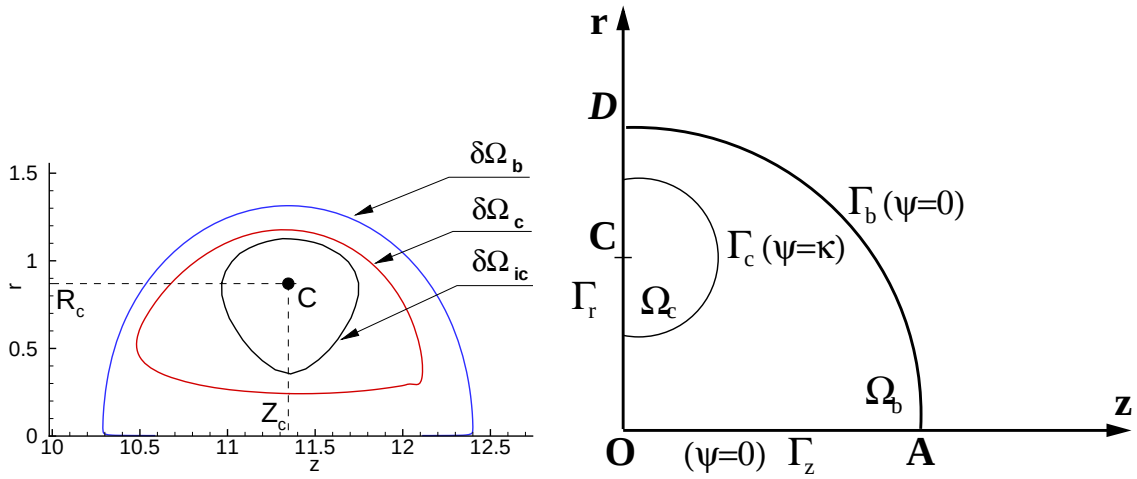

Figure 4.1.: Structure of a vortex ring and domain definition of the mathematical problem of steady vortex rings.

The following constraints are also imposed:

- ψ et $\nabla\psi$ are continuous on $\delta\Omega_c$;
- $\psi = k$ on $\delta\Omega_c$ that has to be a streamline,
- the translation velocity W is equal to the free stream velocity at infinity:

$$\psi + \frac{1}{2}Wr^2 \to 0 \quad \text{for} \quad r^2 + z^2 \to \infty. \tag{4.1.2}$$

The difficulties of the global problem come from the unbounded domain Π, associated with a lack of compactness theorems, and from the fact that $\delta\Omega_c = \Gamma_c$ is a free boundary that has to be calculated. Under certain hypotheses, existence and uniqueness results were obtained by Fraenkel and Berger (1974); Esteban (1983). For more realistic conditions, only mathematical conjectures were formulated (for a discussion, see Berestycki et al., 1984).

From a numerical point of view, the idea to use the software FreeFem++ (`http://www.freefem.org`) for this 2D problem came naturally. This free software is developed in Laboratoire Jacques-Louis Lions by F. Hecht, O. Pironneau and A. LeHyaric. Some of the finite elements numerical algorithms used in FreeFem++ are presented in a simplified form in the book [O3].

FreeFem++ proposes a large variety of triangular finite elements (linear and quadratic Lagrangian elements, discontinuous $P1$, Raviart-Thomas elements, etc.) to solve partial differential equations (PDE) in two dimensions (2D). FreeFem++ is an integrated product with its own high level programming language with a syntax close to mathematical formulations. Among the features making FreeFem++ an easy-to-use and highly adaptive software we recall the advanced automatic mesh generator, mesh adaptation, problem description by their variational formulations, automatic interpolation of data, color display online, postscript printouts, etc.

The general problem is greatly simplified if the boundary Γ_b of the vortex bubble is fixed (Fig. 4.1). As a first step, I have considered elliptic shapes for Γ_b with different aspect ratios. The vortex core $\delta\Omega_c$ is then calculated. The developed numerical algorithm has faster convergence than other published algorithms (Durst et al., 1981). Figure 4.2 illustrates a numerical result obtained for the case $f(\psi) = Cr$, with C a constant; the fast convergence of the algorithm is also shown.

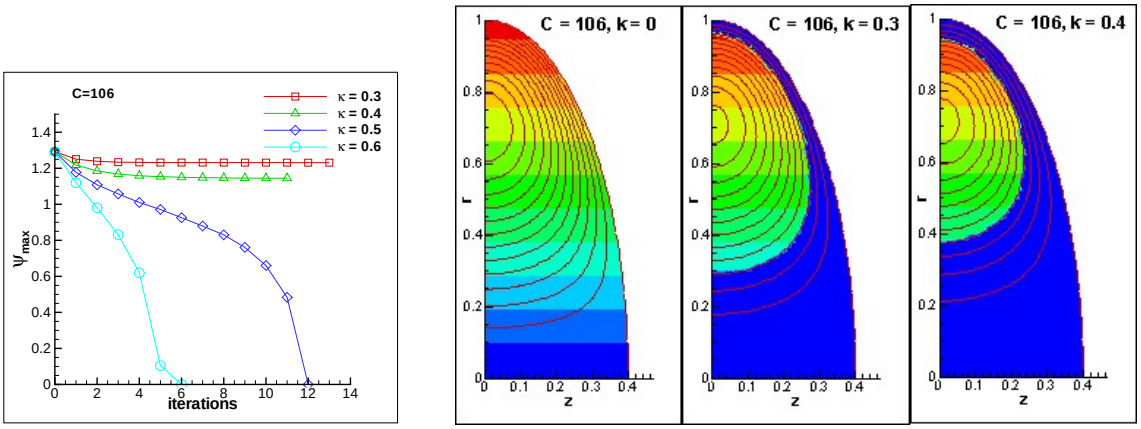

Figure 4.2.: Elliptic steady vortex ring. Convergence history of the algorithm and solutions ψ for different parameters. Simulations with FreeFem++.

The mathematical analysis of this problem will involve collaborations with S. Serfaty (Professor, UPMC) and N. Le (post-doc,University of Columbia, USA). The ongoing work concerns the theoretical estimation of critical parameters defining the domain of existence of non zero solutions for the elliptic vortex problem. These estimations are currently compared to numerical results.

A practical motivation for this study comes from the experimental investigation of industrial flows. Figure 4.3 shows PIV (Particle Image Velocimetry) experimental images of a spray injection. The vortex ring that obviously forms at the top of the

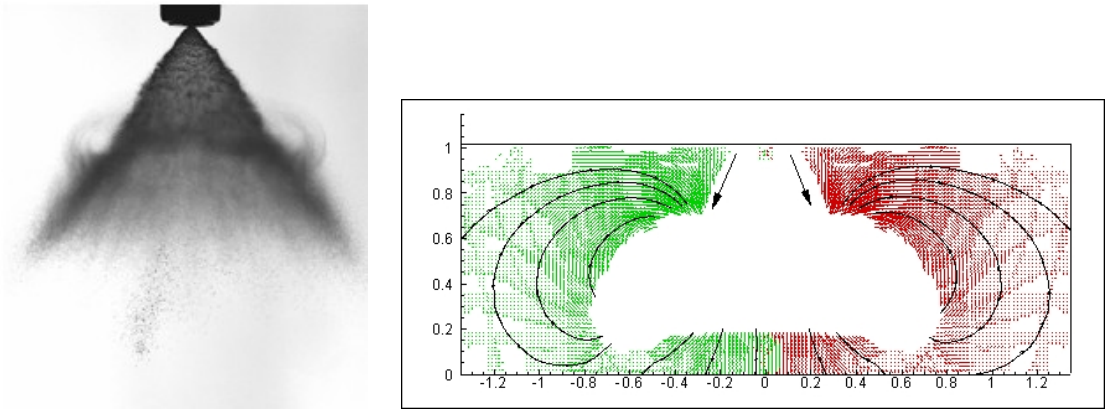

Figure 4.3.: Experimental PIV velocity field in a conical injection two-phase flow (spray). Courtesy of J. Hélie, Continental Automotive France.

jet is not visible because of the large density of spray droplets in this region. The flow inside the spray is not visible and a theoretical reconstruction of the velocity field would be useful for such diagnostics. Such theoretical reconstruction will be based on ideal vortex ring models, calculated numerically and theoretically. Similar problems of (real-time) field reconstruction are encountered in theoretical modeling of plasmas trapped in a Tokamak reactor (see, for instance Blum et al., 2007).

4.2. Numerical and theoretical analysis of the entry region of a pipe flow

Numerical simulation of vortex rings presented in section 3.3 used a model for the imposed velocity profile at the inlet. This model approximates the experimentally measured mean profiles, but does not take into account the time variation of the vorticity layer thickness at the nozzle lip. A more realistic simulation would include in the computational domain the upstream part of the flow that develops in a cylindrical pipe. This approach is time consuming, since the pipe flow has to be correctly resolved. An alternative is to develop new models for the inflow profile by considering the flow developing in the entry region of the pipe. It should be recalled that this region (Fig. 4.4) has completely different behaviour that the well known developed (Poiseuille) region of the pipe flow.

From a numerical point of view, the code JETLES can be easily modified to simulate pipe flows. This work has been already done in collaboration with C. Vadean (PhD student, University Politehnica of Bucarest, Romania). Preliminary results (Fig. 4.5) were validated against existing numerical data and will be used as a data base for the theoretical developments.

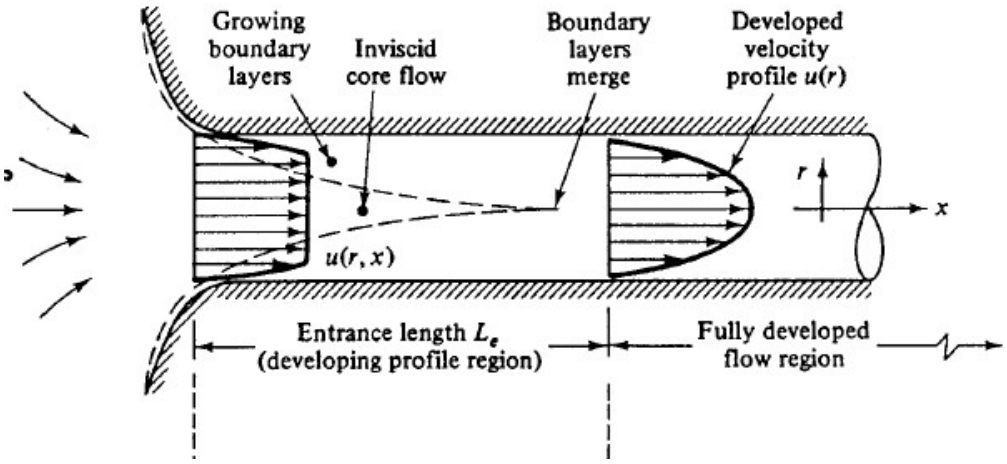

Figure 4.4.: Sketch of the laminar flow in a pipe.

Theoretical modeling is not an easy task since unsteady effects dominate the entry region. Several simplified approaches were proposed in the literature, but analytical descriptions of the velocity profiles depending on the time t and space (r, z) variables are not currently available (see Fargie and Martin, 1971; Das and Arakeri, 1998). This topic will be addressed in a joint research work with S. Danaila (Professor, University Politehnica of Bucarest, Romania).

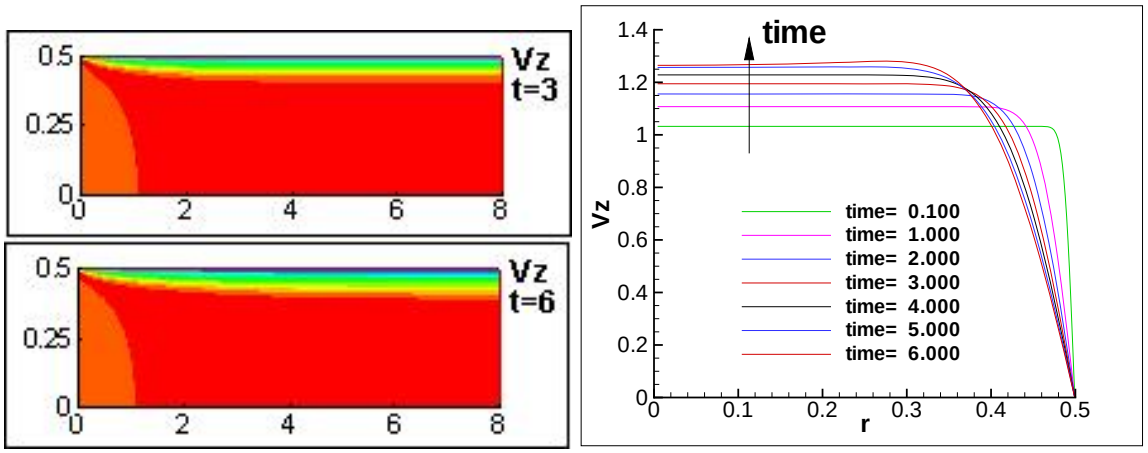

Figure 4.5.: Laminar flow in the entry region of a pipe flow. Iso-contours and profiles of streamwise velocity V_z. Simulation with JETLES.

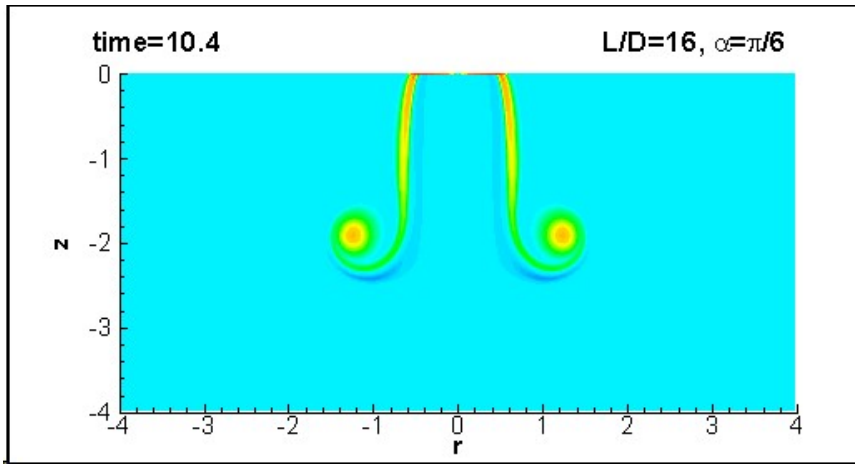

Figure 4.6.: (Animation) Evolution of the vorticity for a conical injection. Simulation with JETLES.

4.3. Numerical simulation of conical injection flows

Further developments of the JETLES code [Code2] will include theoretical analysis (behaviour of high order finite differences, as compact schemes, study of new boundary conditions) and numerical developments (code optimization, MPI parallelization). This academic code, easy to use and modify, will serve as numerical laboratory to test numerical analysis theories. By example, the new theories developed by Sani et al. (2006) and Pironneau and Gresho (2008) on the formulation of boundary conditions for incompressible flows could be numerically tested with this code. This could be interesting since the cited theories correct the classical theory of Gresho and Sani (2000).

A new class of flows will be simulated with JETLES. The conical injection is closer to real configuration in recent automotive internal combustion engines (see Fig. figure 4.3). Conical vortex rings with constant or variable density will be analyzed in collaboration with C. Vadean (PhD student, University Politehnica of Bucarest, Romania). Preliminary results (see animation 4.6) suggests that new physics is to be explored in such configurations.

II

Simulations of superfluids: Bose-Einstein condensates

5. Numerical simulations of vortex configurations in Bose-Einstein condensates

General presentation

This is a recent research activity that I have started in 2001 after a Workshop organized by Amandine Aftalion. The main accomplishment of this work is the development of a numerical code (BETI – *Bose-Einstein en Temps Imaginaire*) that propagates in imaginary time the three-dimensional (3D) Gross-Pitaevskii (GP) equation. The numerically converged states represent critical points of the GP energy. From a physical point of view, these states are equivalent to stable or metastable equilibrium configurations in a Bose-Einstein condensate (BEC). At the time when the very first results were obtained with this code, there were only two studies (García-Ripoll and Pérez-García, 2001) (the preprint of Modugno et al., 2003) using 3D simulations to investigate single vortex configurations in BECs. Even at the present time, there exists few 3D numerical codes (Berloff, 2004; Kasamatsu et al., 2005) for the study of the physics of BECs.

Since numerical methods that directly minimize the GP energy (García-Ripoll and Pérez-García, 2001; Modugno et al., 2003), using conjugate gradient or Sobolev gradients algorithms, proved to be cumbersome in simulating BEC configurations with multiple vortices (dense lattices), I have developed a finite differences method to find critical points of the GP energy by solving the corresponding Euler-Lagrange equation. At this level, I acknowledge useful discussions with Qiang Du (Penn State University) who used finite elements methods to solve the same equation in 2D (Aftalion and Du, 2001).

The new numerical code allows to simulate configurations close to experimental ones. I have generally used physical parameters corresponding to experiments performed in the *Cold Atoms* group of Jean Dalibard from Laboratoire Kastler-Brossel (LKB), École Normale Supérieure Paris. I acknowledge here many stimulating discussions with Jean Dalibard and the members of his group, Vincent Bretin and Sabine Stock. They had the patience to explain physical features of experimental BEC and to propose new configurations to be explored numerically.

This chapter starts with a short description of experimental BEC configurations with vortices. The mathematical model for quantized vortices is introduced, since it is different from that used for vortices in classical fluids. The numerical method used to compute 3D vortex configurations is presented in detail. The next chapter will show some of the numerous results obtained with this method.

Key words: finite differences, compact schemes, Gross–Pitaevskii equation, Bose-Einstein condensate, quantized vortex.

Publications :

articles : [A3], [A6], [A7], [A9], [A10],
numerical codes : [Code1].

Collaborations :

A. Aftalion (CNRS, Lab. Jacques-Louis Lions),
L. C. Crasovan (Universitat Politecnica de Catalunya, Barcelona),
J. Dalibard, S. Stock, V. Bretin (Lab. Kastler Brossel, ENS),
Q. Du (Penn State University, USA),
V. M. Pérez-García (University of Castilla–La Mancha).

5.1. Experimental realisations of Bose-Einstein condensates

Bose Einstein condensates (BEC) owe their name to the prediction of Bose and Einstein in 1925: for a gas of non interacting particles at very low temperature, a macroscopic fraction of the gas is in the state of lowest energy, that is condensed. As a consequence, the atoms in the condensate oscillate following the same complex wave function ψ, which evolution is described by the nonlinear Schrödinger equation.

The first experimental realization of atomic BEC in 1995 was awarded the Nobel Prize in 2001, the laureates being E. A. Cornell (University of Colorado), W. Ketterle (MIT) and Carl E. Wieman (University of Colorado). Since then, a lot of properties of these systems have been studied both experimentally and theoretically (see, for instance, http://www.lkb.ens.fr/-Condensats-de-Bose-Einstein-, http://jilawww.colorado.edu).

In recent years, several experimental studies proved the superfluidity of BECs by putting into evidence different properties related to this state, as the appearance of a permanent current when moving a laser beam in a condensate (Raman et al., 1999), or the nucleation of quantized vortices when rotating the condensate (Madison et al., 2000, 2001; Abo-Shaeer et al., 2001). The second approach was used in the experiments performed by the *Cold Atoms* group in Laboratoire Kastler-Brossel (LKB), École Normale Supérieure (ENS). These experiments will be described in the following.

The condensate is typically confined by a magnetic potential and set into rotation using a laser beam, which can be assimilated to a spoon stirring a cup of tea (see Fig. 5.1). Since the solid body rotation is not possible in a superfluid system, the condensate has the choice between staying at rest and rotating by nucleating quantized vortices. The number and shape of vortices depend on the rotational frequency and the geometry of the trap. In ENS experiments, the trapping frequency ω_z is much smaller than ω_x and ω_y, which explains the cigar shape of the condensate. Typical size of the condensate is 100 μm for the length and 10 μm for the diameter.

Quantized vortices start to nucleate in the condensate when the rotation frequency Ω exceeds a critical value Ω_c. If the condensate is described by the macroscopic wave function

$$\psi = \sqrt{\rho(x,y,z)}\, e^{i\theta(x,y,z)}, \tag{5.1.1}$$

where ρ is the local density and θ the phase, a quantized vortex is a topological

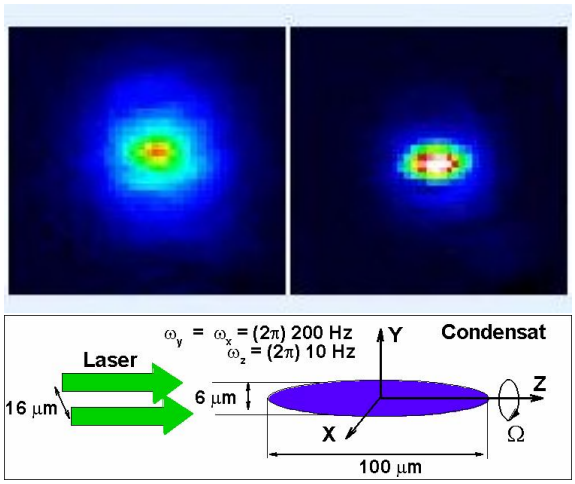

Figure 5.1.: Experimental realization of a BEC in Laboratoire Kastler-Brossel and sketch of the configuration with rotating cigar-shape condensate (see also http://www.lkb.ens.fr).

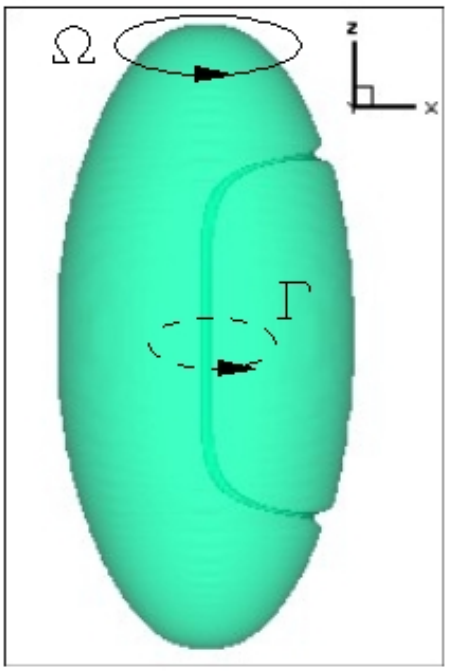

Figure 5.2.: (Animation) Numerical simulation of a singly quantized vortex in a cigar-shape condensate. Identification by means of iso-surface of low density $\rho = |\psi|^2$.

defect of ψ. In other words, $\rho = 0$ in the core of the vortex (there are no atoms) and around the vortex there exists a frictionless superfluid flow with a discontinuous phase field. Therefore, if the local velocity in a point, with non-zero density, is defined, by analogy with classical fluids, as

$$\mathbf{v} = \frac{h}{2\pi m}\nabla\theta = \frac{\hbar}{m}\nabla\theta, \tag{5.1.2}$$

the circulation around a vortex will be quantized (Fig. 5.2)

$$\Gamma = \oint \mathbf{v}.\mathbf{d}l = n\frac{h}{m}, \tag{5.1.3}$$

where h is the Planck's constant, m the atomic mass and n an integer. The quantification of the circulation is a striking feature of superfluid vortices compared to vortices in classical fluids. The flow around a vortex is also called *super-current*.

This description suggests a simple method for the identification of vortices in numerical simulations by plotting iso-surfaces of low density $\rho = |\psi|^2$, as shown in Fig. 5.2 for a singly quantized vortex ($n = 1$). The integer n is evaluated by counting phase discontinuities around the vortex line. This method also visualize the boundary of the condensate, since the atomic density goes to zero out of the magnetic trap. It is interesting to note in passing that in classical fluid dynamics there are still controversial debates on the general definition of a vortex.
For the trapping potentials considered in the following, only singly quantized vortices are obtained. When increasing $\Omega > \Omega_c$, more and more vortices appear and arrange themselves into a regular triangular (Abrikosov) lattice, as seen in Fig. 5.3.
Because of the small dimensions of the BEC, the details of each vortex line is difficult, and sometimes impossible, to observe from experimental visualizations. This recalls the interest in 3D numerical simulations to investigate such configurations.

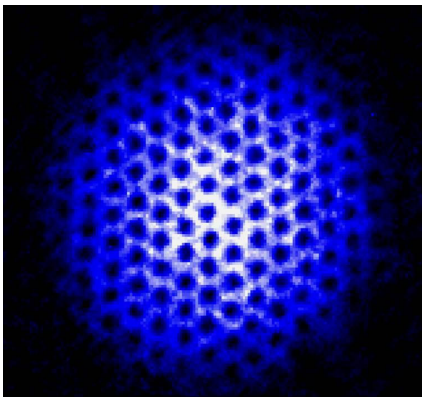

Figure 5.3.: Abrikosov lattice of vortices in a BEC. Experiments performed in JILA, University of Colorado (http://jilawww.colorado.edu).

5.2. Theoretical model

The condensates obtained from alkali gases are characterized by a uniform density imprinted by the trapping potential that confines the atoms. In the same time, the condensates are diluted, and the interactions between atoms are week. As a consequence, a good mathematical description is to consider that all the atoms are described by the same wave function that obeys the nonlinear Schrödinger equation, with a supplementary term taking into account the trapping potential.

We consider a pure BEC of N atoms confined in a trapping potential V_{trap} rotating along the z axis at angular velocity Ω. The energy of the system in the rotating frame is described by the Gross-Pitaevskii (GP) functional:

$$\mathcal{E}(\psi) = \int_{\mathcal{D}} \frac{\hbar^2}{2m}|\nabla\psi|^2 + V_{trap}\,|\psi|^2 + \frac{N}{2}g_{3D}|\psi|^4 - \hbar\mathbf{\Omega}\cdot(i\psi, \nabla\psi \times \mathbf{x}), \qquad (5.2.1)$$

where we denote by $\mathbf{\Omega} = \Omega\mathbf{e}_z$, the rotation frequency. The interaction coefficient is defined as $g_{3D} = 4\pi\hbar^2 a_s/m$, where a_s is the scattering length. The wave function

is normalized to unity, *i.e.* $\int_{\mathcal{D}} |\psi|^2 = 1$. The trapping potential has usually the harmonic form:

$$V_{trap}(x, y, z) = \frac{1}{2} m \left(\omega_x^2 x^2 + \omega_y^2 y^2 + \omega_z^2 z^2 \right), \tag{5.2.2}$$

with $\omega_{x,y,z}$ the trap frequencies along each spatial direction. We shall see in the following other types of trapping potentials used in experiments. In equation (5.2.1), the first term is the kinetic energy, the second comes from the trapping interactions, the third is the atomic interactions term, and the last is introduced by the change of frame.

An important mathematical work on this model was provided in Laboratoire Jacques-Louis Lions by A. Aftalion and her collaborators (Aftalion and Du, 2001; Aftalion and Jerrard, 2002; Aftalion and Riviere, 2001). For theoretical and numerical analysis, it is convenient to use the scaling introduced in Aftalion and Riviere (2001):

$$d = \left(\frac{\hbar}{m\omega_x} \right)^{1/2}, \ \varepsilon = \left(\frac{d}{8\pi N a} \right)^{2/5}, \ R = \frac{d}{\sqrt{\varepsilon}}, \tag{5.2.3}$$

$$\mathbf{r} = \mathbf{x}/R, \ u(\mathbf{r}) = R^{3/2}\phi(\mathbf{x}),$$

$$\tilde{\Omega} = \Omega/(\varepsilon\omega_x), \ \alpha = \omega_y/\omega_x, \ \beta = \omega_z/\omega_x.$$

The 3D dimensionless energy becomes

$$E(u) = H(u) - \tilde{\Omega} L_z(u), \tag{5.2.4}$$

where H is the Hamiltonian

$$H(u) = \int \frac{1}{2}|\nabla u|^2 + \frac{1}{2\varepsilon^2} V(\mathbf{r})|u|^2 + \frac{1}{4\varepsilon^2}|u|^4, \tag{5.2.5}$$

V the dimensionless potential and L_z the angular momentum

$$L_z(u) = i \int \bar{u} \left(y \frac{\partial u}{\partial x} - x \frac{\partial u}{\partial y} \right). \tag{5.2.6}$$

The equilibrium of the system corresponds to minima of the Gross-Pitaevskii energy. The small parameter ε plays the role of asymptotic parameter for the study of the condensate in the Thomas-Fermi regime. Mathematical analysis usually consider the problem of finding minima of $E(u)$ for different Ω, proving if the minimum displays vortices in the condensate and describing the shape and position of such vortices. For a recent revue of the mathematical work in this area, see the recent book by Amandine Aftalion (Aftalion, 2006).

5.3. Numerical approach

Critical points of $E(u)$ may be computed in several ways: either by directly minimizing the energy functional using conjugate-gradient algorithms (Modugno et al., 2003) or Sobolev gradients techniques (García-Ripoll and Pérez-García, 2001), or by solving the corresponding Euler-Lagrange. In this study, we use the second approach because of its ability in simulating 3D configurations with multiple vortices in the condensate

The Euler-Lagrange equation derived from (5.2.4) is propagated in *imaginary time* (by adding the term $\partial u/\partial t$) until convergence to a steady state corresponding to equilibrium configurations of the condensate. Consequently, the numerical algorithm solves the PDE equation:

$$\frac{\partial u}{\partial t} - \frac{1}{2}\nabla^2 u + i(\tilde{\mathbf{\Omega}} \times \mathbf{r}).\nabla u = -\frac{1}{2\varepsilon^2}u(V + |u|^2) + \mu_\varepsilon u, \tag{5.3.1}$$

on a spatial domain $\mathcal{D}$, with homogeneous boundary conditions $u = 0$ on $\partial\mathcal{D}$. The Lagrange multiplier μ_ε is computed in order to respect the unitary norm constraint, $\int_\mathcal{D} |u|^2 = 1$,

$$\mu_\varepsilon = \int_\mathcal{D} \left\{ \frac{1}{2}|\nabla u|^2 + \frac{1}{2\varepsilon^2}(V + |u|^2)|u|^2 \right\} - \tilde{\mathbf{\Omega}} L_z.$$

The computational domain is rectangular (see Fig. 5.4). The size of the computational domain is estimated from the theoretical Thomas-Fermi (TF) density distribution law:

$$\rho_{\mathrm{TF}}(r,z) = \frac{m}{4\pi\hbar^2 a_s}\left(\mu - V_{trap}(r,z) + \frac{1}{2}m\Omega^2 r^2\right), \tag{5.3.2}$$

where $r = \sqrt{x^2+y^2}$ and μ is the chemical potential analytically calculated from the constraint:

$$\int_{\{\rho_{\mathrm{TF}}>0\}} \rho_{\mathrm{TF}}(\mathbf{r}) = 1. \tag{5.3.3}$$

The maximum transverse radius $R_\perp$ and longitudinal half-length R_z of the condensate can be then calculated from (5.3.2). In fact, the computational domain has to be larger in order to allow the relaxation to zero of the wave function on the border $\partial\mathcal{D}$.

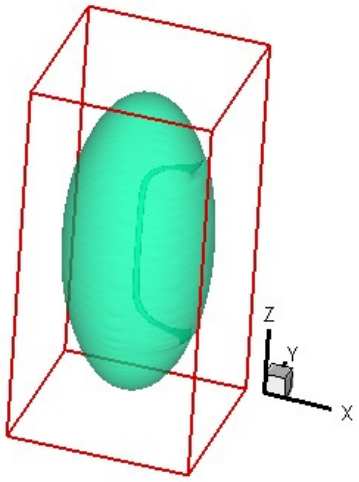

Figure 5.4.: Computational domain.

The PDE (5.3.1) is propagated in imaginary time by a hybrid 3 steps Runge-Kutta-Crank-Nicolson scheme, inspired from my work in *classical fluids* simulations (see also section 3.1):

$$\frac{u_{l+1}-u_l}{\delta t} = a_l\mathcal{H}_l + b_l\mathcal{H}_{l-1} + c_l\nabla^2\left(\frac{u_{l+1}+u_l}{2}\right), \tag{5.3.4}$$

where $\mathcal{H}$ contains the remaining non-linear terms. The corresponding constants for every step ($l = 1, 2, 3$),

$$a_1 = \frac{8}{15}, a_2 = \frac{5}{12}, a_3 = \frac{3}{4}, b_1 = 0, b_2 = -\frac{17}{60}, b_3 = -\frac{5}{12}, c_1 = \frac{8}{15}, c_2 = \frac{2}{15}, c_3 = \frac{1}{3},$$

are analytically found in order to obtain a second order scheme in time. The resulting semi-implicit scheme allows reasonably large time steps, making it appropriate for the long time integration necessary to check the stability of the equilibrium configuration. The large linear systems with sparse matrices resulting from the implicit terms are solved by an alternating direction implicit (ADI) factorization technique. Final linear systems with tridiagonal matrices are solved by an optimized direct LU algorithm.

For the spatial discretization we use finite differences on a Cartesian uniform mesh. To accurately resolve sharp gradients of the variable in presence of vortices, low numerical dissipation and very accurate schemes are required for the spatial derivatives. A sixth-order compact finite difference scheme with spectral-like resolution was chosen to this end.

Compact schemes are based on implicit relationships between the discrete values of derivatives. These values are computed for all grid points in one direction by inverting a linear system. Several families of implicit finite differences schemes are derived in Lele (1992). The most popular are the compact (or Padé) schemes that allows to get sixth-order accuracy using a three-point stencil only. For this scheme, the first and second derivatives at the grid point i, far from the boundaries, are computed from:

$$\frac{1}{3}u'_{i-1} + u'_i + \frac{1}{3}u'_{i+1} = \frac{14}{9}\frac{u_{i+1}-u_{i-1}}{2\delta x} + \frac{1}{9}\frac{u_{i+2}-u_{i-2}}{4\delta x}, \tag{5.3.5}$$

$$\frac{2}{11}u''_{i-1} + u''_i + \frac{2}{11}u''_{i+1} = \frac{12}{11}\frac{u_{i+1}-2u_i+u_{i-1}}{\delta x^2} + \frac{3}{11}\frac{u_{i+2}-2u_i+u_{i-2}}{4\delta x^2}, \tag{5.3.6}$$

where δx is the (constant) grid step. Another advantage of these schemes is their spectral-like behavior (no numerical dissipation and good spectral resolution).

The grid is uniform in all three space directions. Convergence tests are made for each run in order to fix the grid density. For high rotation frequencies Ω (when the condensate is nearly spherical and more than 100 vortices are present), up to $240 \times 240 \times 240$ grid points are used to compute equilibrium states.

It is worth at this point to describe how the condensate evolves in "imaginary" time (i.e. how it relaxes to an equilibrium state). A typical simulation starts either from an initial condition (ground state) with no vortices in the condensate, or from an artificial field obtained by superimposing to the ground state a simplified model for vortices. The ground state corresponds to the TF density distribution (5.3.2) for a given trapping potential V_{trap}. When solution branches are followed, the converged field for lower Ω is used as initial condition. When suddenly increasing Ω, new vortices are generated at the border of the condensate and enter the condensate. In the first stages of the computation, 3D vortex lines are strongly distorted, giving a *spaghetti* image of the lattice (see Fig. 5.5). Close to equilibrium, vortices become straight in their central part and arrange themselves in a more and more regular lattice (Fig. 5.5). Convergence is particularly slow at the end of the computation when the position and shape of vortices evolve very slowly. Convergence is considered when the energy remains constant (relative fluctuations $|\delta E/E|$ less than 10^{-6}) for a relatively long time to be sure that a stable state was obtained. The convergence time is longer for high values of the rotation frequency (the lattice continues to slowly evolve, with minor changes in the vortex positions).

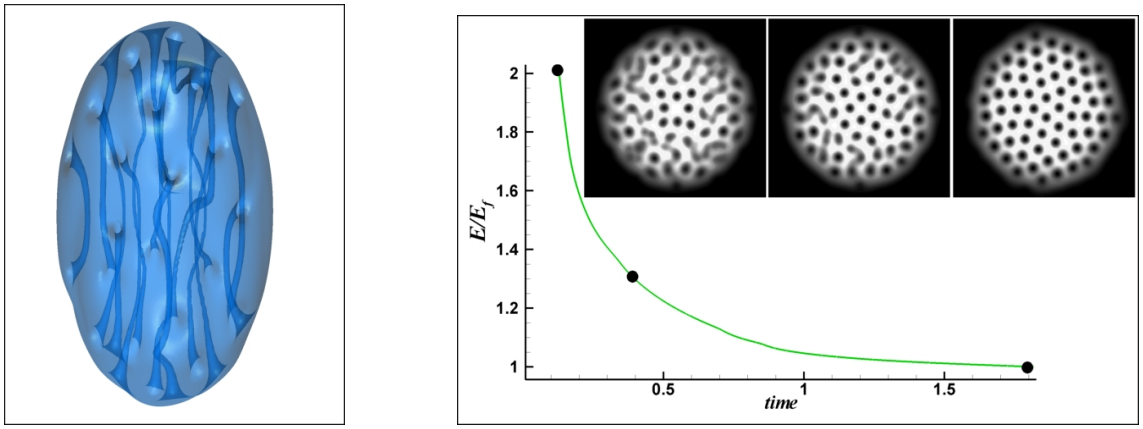

Figure 5.5.: Illustration of the convergence of an *imaginary time* numerical simulation. Spaghetti-like vortex structure in the condensate before convergence to an equilibrium state (iso-surface of low density $\rho = |\psi|^2$). Example of energy decrease during the propagation of 3D Gross-Pitaevskii equation in imaginary time. Energy is normalized by the equilibrium (final) value E_f. Inserts show iso-contours of the integrated (along z) density corresponding to three successive time instants represented on the energy curve.

As a final remark, we have to emphasize the fact that the present numerical method is well adapted to the imaginary time propagation of the GP equation (which can be regarded in this context as a heat equation with complex variables). The numerical scheme displays the requested property of diminishing the energy of the system, as described in Bao and Du (2004). For the real-time propagation of the GP equation (with the term $i\partial u/\partial t$ instead of $\partial u/\partial t$), different algorithms that conserve energy (see Bao and Du, 2006) have to be used.

6. Three-dimensional structure of quantized vortices in a Bose-Einstein condensate

General presentation

We present in this chapter the main results obtained using the numerical approach described in the previous chapter. This work was motivated by recent experimental achievements of rotating BECs by the École Normale Supérieure (ENS) group of Jean Dalibard. We have tried, not only to reproduce their experimental configurations, but also to suggest new ones resulting from the theoretical analysis of our numerical results.

We describe in detail the three-dimensional structure of vortices for different trapping potentials used in experiments. Our simulations offer a detailed 3D picture of vortex configurations that is not available from experiments and 2D simulations. A particular attention was devoted to the physical interpretation of the results by using post-processing diagnostics close to experimental ones. Numerical data are always compared to available experimental and theoretical results and a remarkably good qualitative and quantitative agreement is found.

A rich variety of vortex configurations are illustrated in this chapter, from single-line vortices to Abrikosov lattices and giant vortices, depending on the trapping potential and the rotation frequency. The gallery of vortex structures that will be shortly presented in the following (more details can be found in the published papers, recalled for each item) will include:

- singly quantized vortex, which may take a U, a S shape, or a 3D-S shape, in a condensate with harmonic trapping potential; this is the case considered in most experimental and theoretical studies; (Aftalion and Danaila, 2003);
- giant vortex, obtained for weak rotation frequencies when a *quartic-minus-quadratic* potential is used to trap the condensate; this configuration was not yet studied experimentally ; (Aftalion and Danaila, 2004);
- vortex latices and giant vortex in fast rotating condensates trapped by a

quartic-plus-quadratic potential; this numerical configuration used exactly the experimental parameters and allowed to go beyond experimental observations, since experiments failed to reach rotation frequencies to obtain giant vortices; (Danaila, 2005);

- vortices with *exotic* shapes (vortex stars, parallel vortex lines, parallel vortex rings, etc.) that we have imagined in non rotating condensates; these configuration could be realized by new phase-engineering capabilities developed in experiments; (Crasovan et al., 2004).

A very new configuration that is currently under consideration consists in a rotating condensate in 1D optical lattices. Some preliminary numerical results for this configuration will be presented in the next chapter describing my research program in this field.

Key words: Bose-Einstein condensate, quantized vortex, giant vortex, vortex lattice.

Publications :
articles : [A3], [A6], [A7], [A9], [A10],
numerical codes : [Code1].

Collaborations :
A. Aftalion (CNRS, Lab. Jacques-Louis Lions),
L. C. Crasovan (Universitat Politecnica de Catalunya, Barcelona),
J. Dalibard, S. Stock, V. Bretin (Lab. Kastler Brossel, ENS),
Q. Du (Penn State University, USA),
V. M. Pérez-García (University of Castilla–La Mancha).

6.1. Single vortex lines in rotating BECs

In experiments, the condensate is typically confined by the harmonic (quadratic) potential given by (5.2.2). This type of potential was used to experimentally study single vortex lines in a prolate condensate (Madison et al., 2001; Rosenbusch et al., 2002; Bretin, 2004). Experimental evidence was provided to prove that the vortex line is not straight along the axis of rotation, but bending. The vortex displays therefore a U shape. More complicated configurations (S vortices) were also observed in experiments (see Fig. 6.1).

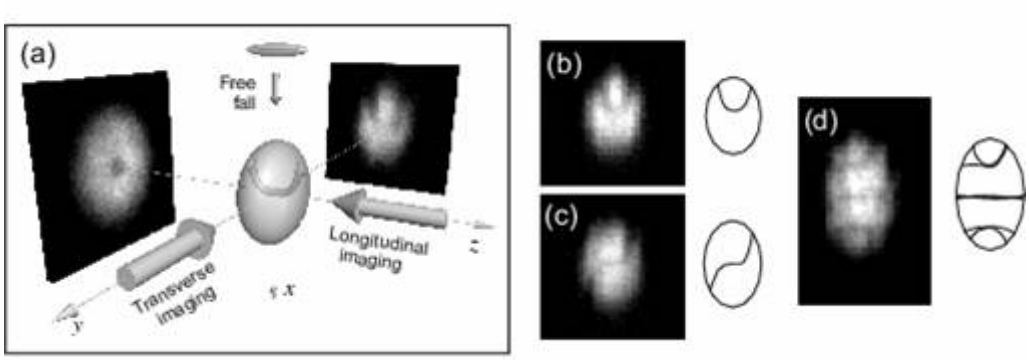

Figure 6.1.: Single line vortex configurations observed in experiments (Rosenbusch et al., 2002).

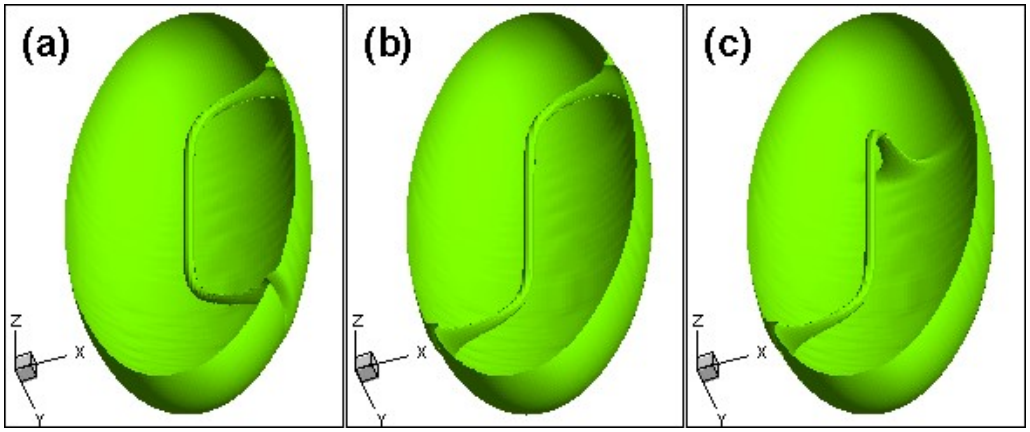

Figure 6.2.: Single vortex lines in a prolate rotating condensate with harmonic trapping potential: U vortex (a), planar S vortex (b) and non-planar S vortex (c). Iso-surfaces of low density $\rho = |u|^2$.

The numerical parameters are set accordingly to ENS experiments. The dimensionless potential (5.2.2) becomes:

$$V = x^2 + \alpha^2 y^2 + \beta^2 z^2, \tag{6.1.1}$$

with $\alpha = 1.06, \beta = 0.067$, corresponding to physical values:

$$m = 1.445{\cdot}10^{-25}\,[kg], \quad a_s = 5.8{\cdot}10^{-9}\,[m], \quad N = 1.4{\cdot}10^{5}, \quad \omega_x = 1094\,[s^{-1}].$$

The small parameter ε is set to 0.02. The angular frequency Ω is varied from 0 to the maximum value of $0.9\omega_x$, *i.e.* $\tilde{\Omega} \in [0, 0.9[$. A typical numerical simulation starts from an initial condition defined by a Thomas-Fermi density distribution (condensate without vortex) – the rotation frequency is then suddenly increased to get equilibrium states with vortices. Some simulations starts from a simple ansatz describing condensates with 3D vortex lines inside.

For example, an initial condition with a centered straight vortex of radius ε is obtained by imposing:

$$u(x, y, z) = \sqrt{\rho_{\mathrm{TF}}} \cdot u_\varepsilon, \tag{6.1.2}$$
$$u_\varepsilon = \sqrt{0.5 \left\{ 1 + \tanh\left[\frac{4}{\varepsilon} (r - \varepsilon) \right] \right\}} \cdot \exp(i\varphi),$$

where (r, φ) are the polar coordinates in the (x, y) plane. The 3D shape of the vortex can be easily modified by shifting the center r_0 of the vortex in successive (x, y) planes; for instance, to obtain a planar S shape vortex, the following function can be used:

$$r_0(z) = \begin{cases} -1 + \tanh\left[\alpha_v \left(1 + \frac{z}{\beta_v}\right)\right] \Big/ \tanh(\alpha_v), & z < 0 \\ 1 + \tanh\left[\alpha_v \left(-1 + \frac{z}{\beta_v}\right)\right] \Big/ \tanh(\alpha_v), & z \geq 0. \end{cases}$$

The constants α_v, β_v control, respectively, the curvature and the height of the vortex.

Our numerical simulations reproduce remarkably well vortex shapes observed experimentally (Fig. 6.2). The U vortex was numerically obtained by starting the simulation from an initial condition containing a straight vortex away from the z axis. For a relatively large value of the rotation frequency, the final steady state (*i.e.* the local minimum of the GP energy) displays a planar U shape with a straight central part on the z axis and an outer part reaching the condensate boundary perpendicularly.

The U vortex exists for the range $\tilde{\Omega} \in [0.42, 0.86]$. When varying $\tilde{\Omega}$ at the lower bound, the U vortex disappears and a vortex-free configuration is obtained, while at the higher bound the U vortex degenerates in a three-vortex configuration. As a consequence of the anisotropy of the trap, the branches of the U vortex lies either in the $x - z$ or $y - z$ plane. These characteristics confirm the theoretical predictions (Aftalion and Riviere, 2001; Aftalion, 2006) based on the minimization of the approximate GP energy for a vortex line.

Planar S vortices similar to those displayed in experimental pictures (see Fig. 6.1) were numerically obtained (see Fig. 6.2b) from artificial generated initial conditions containing such a vortex. We checked that the final steady state for a given $\tilde{\Omega}$ is always the same (different initial planar S shapes evolved to the same final configuration). The S vortex exists for all values of $\tilde{\Omega}$ – they are only local minima of the GP energy. An animation showing the structure of this vortex is shown in Fig. 6.3.
We also obtained S vortices with the bent arms rotated by 90 degrees (see Fig. 6.2c). We could check that non planar S configurations with an angle between the branches different from 90 degrees, do not exist. For a given $\tilde{\Omega}$, the three configurations (U, S and 3D-S) are topologically equivalent by a z-rotation of the bent arms of the vortices: the U vortex has a slightly lower energy that the others.

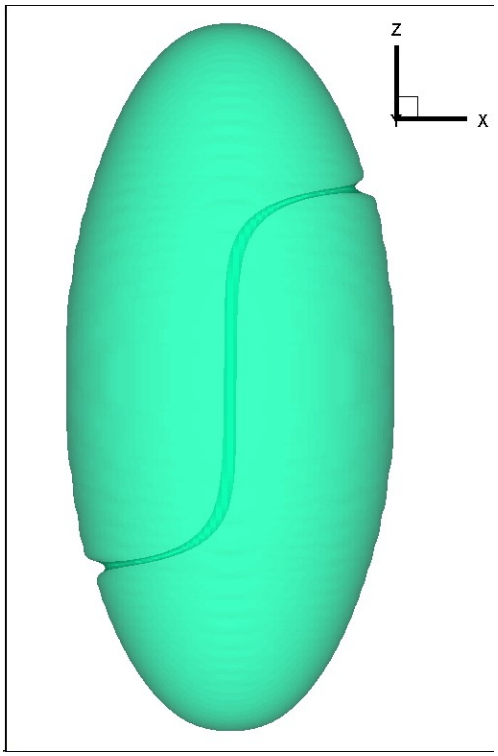

Figure 6.3.: (Animation) S-vortex in a rotating BEC.

Solution branches with two, three or four vortices in the condensate were also obtained by abruptly increasing $\tilde{\Omega}$ to a very large value; these configurations are described in Aftalion and Danaila (2003).

6.2. Giant vortex in rotating BECs

6.2.1. Theoretical study

The harmonic trapping potential (5.2.2) allows for rotation frequencies lower than ω_x; for $\Omega = \omega_x$ the centrifugal force compensates the trapping force and the confinement of the atoms vanishes. The fast rotation regime, corresponding to $\Omega \gtrsim \omega_x$, is the focus of a lot of attention since new physical phenomena are expected.

The experimental approach to reach the fast rotation regime explored by the ENS group (Bretin et al., 2004; Stock et al., 2005; Bretin, 2004) consists in modifying the quadratic (harmonic) trapping potential by superimposing a blue detuned laser beam to the magnetic trap holding the atoms. The resulting *Gaussian-plus-quadratic* potential removes the singularity at the limit $\Omega = \omega_x$ and allows to reach rotation rates up to $\Omega \simeq 1.05\omega_x$:

$$V_{trap}(r,z) = \frac{1}{2}m(\omega_\perp^{(0)})^2(x^2+y^2) + \frac{1}{2}m\omega_z^2 z^2 + U_0\, e^{-2r^2/w^2}, \tag{6.2.1}$$

with $r^2 = x^2 + y^2$ and physical parameters:

$$\omega_\perp^{(0)} = 2\pi{\cdot}75.5\,[Hz], \quad \omega_z = 2\pi{\cdot}11\,[Hz], \quad w = 25\,[\mu m], \quad U_0 = k_B{\cdot}90\,[nK],$$

where k_B is the Boltzmann constant. For r/w sufficiently small, the potential $V(r)$ can be approximated by:

$$V = (1-\alpha)r^2 + \frac{1}{4}kr^4 + \beta^2 z^2. \tag{6.2.2}$$

The centrifugal force makes that the effective trapping potential for the rotating condensate is decreased to:

$$V_{eff} = (1-\alpha)r^2 - \varepsilon^2\tilde{\Omega}^2 r^2 + \frac{1}{4}kr^4 + \beta^2 z^2. \tag{6.2.3}$$

In Aftalion and Danaila (2004) we have theoretically analyzed possible vortex configurations corresponding to the trapping potential (6.2.2). Depending on the choice of α, the Thomas-Fermi density profile for the non-rotating ($\tilde{\Omega} = 0$) condensate can display three different shapes, as shown in Fig. 6.4:

(1) the weak attractive case, obtained for $\alpha < 1$: this is the case closest to experiments and is strongly influenced by the (positive) harmonic part. For $\tilde{\Omega} = 0$, a classical prolate condensate is obtained (Fig. 6.4-1).

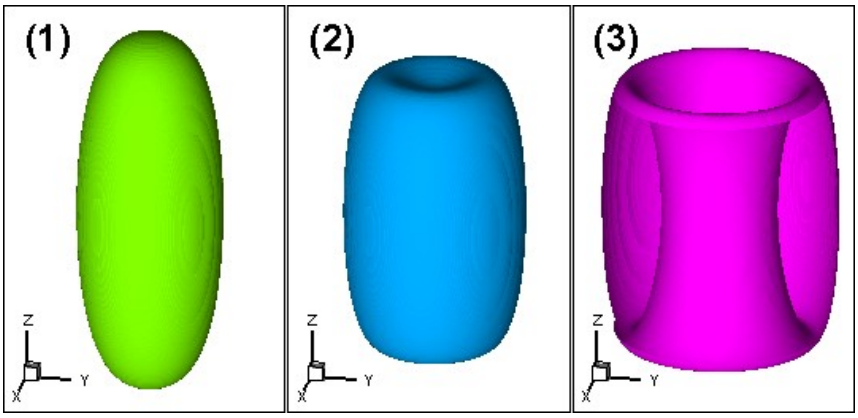

Figure 6.4.: Different shapes of the condensate for the trapping potential (6.2.2). Thomas-Fermi density distribution at $\tilde{\Omega} = 0$ for $\alpha = 0.9$ (picture 1), 1.1 (picture 2), 1.2 (picture 3). These configurations were used as initial conditions for the imaginary time simulations.

(2) the intermediate repulsive case, obtained when $1 < \alpha < 1 + \xi$, with $\xi = \beta^{1/4} k^{5/8}/\sqrt{\pi}$: at $\tilde{\Omega} = 0$, as an imprint of the negative harmonic part, the density profile has a depletion close to the center but no hole (Fig. 6.4-2).

(3) the strong repulsive case, corresponding to $\alpha > 1 + \xi$: the density profile has a hole for all $\tilde{\Omega}$.

The experiments correspond to the first regime. As $\tilde{\Omega}$ increases, the effective trapping potential (6.2.3) starts to have a Mexican hat structure. An Abrikosov vortex lattice appears for intermediate values of $\tilde{\Omega}$; for very large $\tilde{\Omega}$, the theory predicts the appearance of a central hole in the condensate, also called giant vortex. This type of vortex, obtained in our simulations, has not yet been observed in experiments because of the instability of the experimental system for very large rotation rates.

We have numerically proved in Aftalion and Danaila (2004) that the trapping potential corresponding to the second regime allows to obtain a giant vortex in the condensate for lower rotation frequencies. This could be realized by increasing the amplitude U_0 of the detuned laser beam (see equation 6.2.1). The animations 6.5 show how the giant vortex appears in the condensate when the rotation frequency is increased. Each animation describes the converged (equilibrium) configuration for a given $\tilde{\Omega}$. The condensate has initially a Mexican hat structure. When progressively increasing $\tilde{\Omega}$, a vortex lattice is formed and, finally, central vortices merge into a giant vortex. This process, proved to be highly three-dimensional, is clearly observed, which is not the case in experiments. The giant vortex can be regarded as the region containing singly quantized vortices with such low density that they are discernible only by the phase defects.

It is interesting to note that vortex merging leading to the central hole does not involve all the singly quantized vortices in the condensate – an array of such vortices persists around the hole. The observations were confirmed by later theoretical studies (see, for instance Kim and Fetter, 2005).

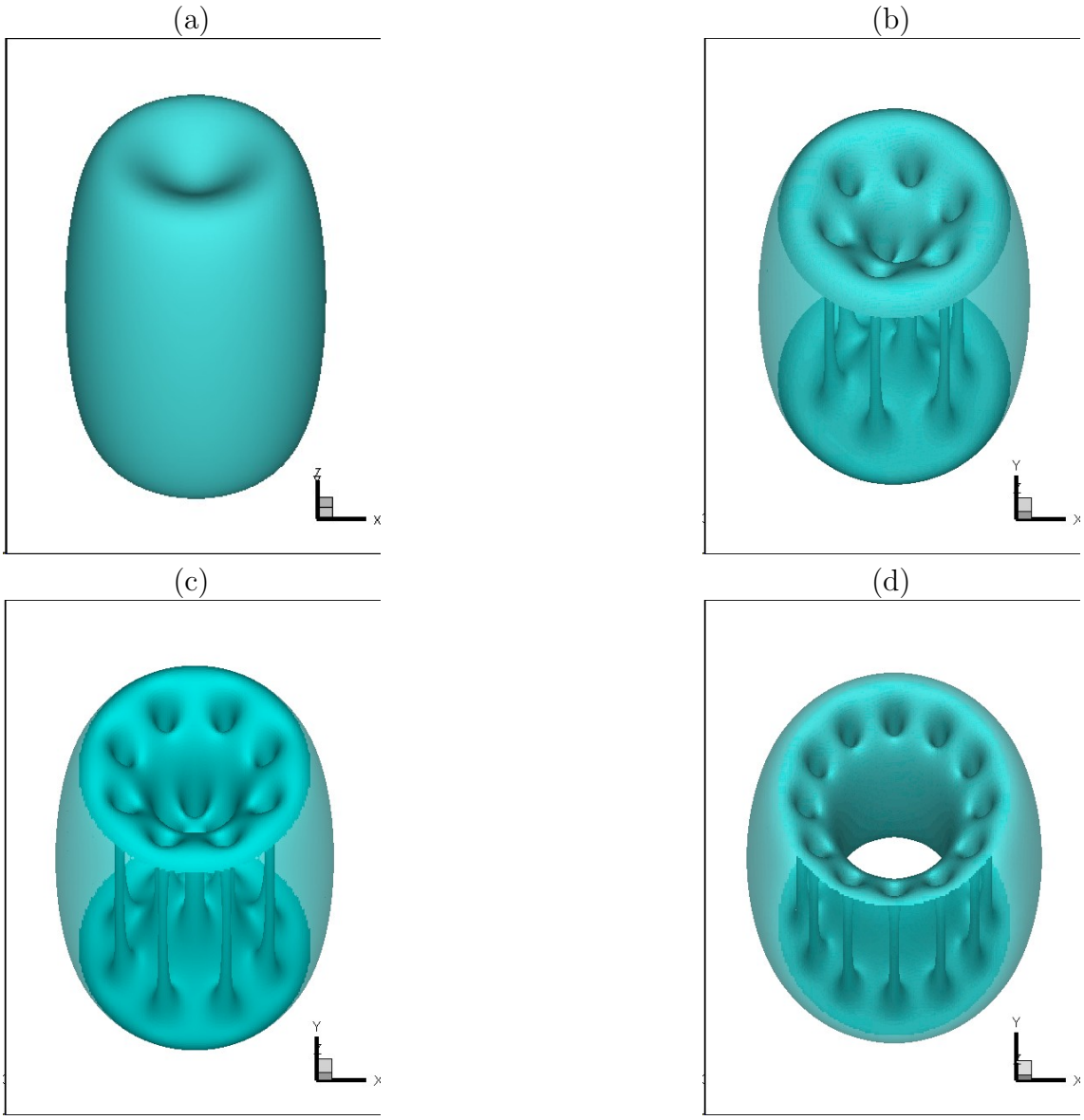

Figure 6.5.: (Animations) Appearance of a giant vortex in a condensate trapped in a *quartic-minus-quadratic* potential. Each animation corresponds to converged (equilibrium) configuration for a given rotation frequency $\tilde{\Omega}$. Increasing values of $\tilde{\Omega}$ from a) to d).

6.2.2. Comparison with experiments

I have also addressed the challenging proposition of using real experimental parameters (Bretin et al., 2004; Stock et al., 2005) in a three-dimensional numerical simulation of fast rotating Bose-Einstein condensates. The experimental pictures (Fig. 6.6) show a very dense vortex lattice that becomes unstable for very large rotation frequencies. Numerical simulations of such configurations, containing around one hundred vortices, request refined computational grids and long integration times because of the slow convergence rates. The code BETI was again optimized in order to deal with grid resolutions of 240^3 ($\sim$ 14 millions) grid points. A typical simulation for this case takes approximately one week on a single processor computer.

The numerically generated 3D-condensates can be seen in Fig. 6.7. The results (Danaila, 2005) reproduce experimental pictures (Fig. 6.6) for rotation frequencies allowing clear experimental observations. For increasing rotation frequencies, the vortex lattice evolves to a vortex array with hole, which confirms the scenario theoretically predicted and also observed in 2D simulations. Since such transition was not observed in experiments, we have qualitatively analyzed the obtained vortex states, with a particular emphasize on the 3D features of vortex merging leading to a central hole in the condensate.

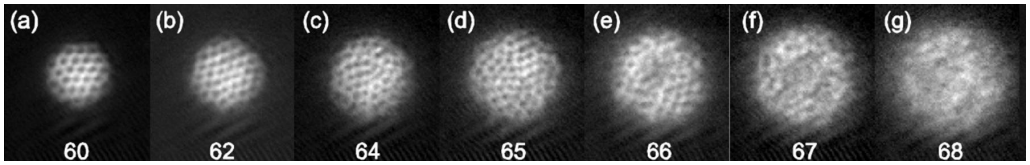

Figure 6.6.: Experimental pictures of a fast rotating BEC (Bretin et al., 2004).

Interesting quantitative information could also be extracted from these simulations. I have developed for this purpose Matlab post-processing tools that allows to automatically compute the characteristics of the vortex lattice, namely the inter-vortex spacing b_v and the vortex core size r_v. Since contrast images (lower row in Fig. 6.7) are the inputs for these programs, they could be also used to analyze experimental pictures.

I found that r_v scales with the healing length $\xi = \sqrt{8\pi a_s \rho}$, as is usually assumed in theoretical studies. The variation of b_v with the distance to the center of the condensate describes the vortex lattice inhomogeneities; a remarkably good agreement is found with the theoretical findings of Sheehy and Radzihovsky (2004) (Fig. 6.8).

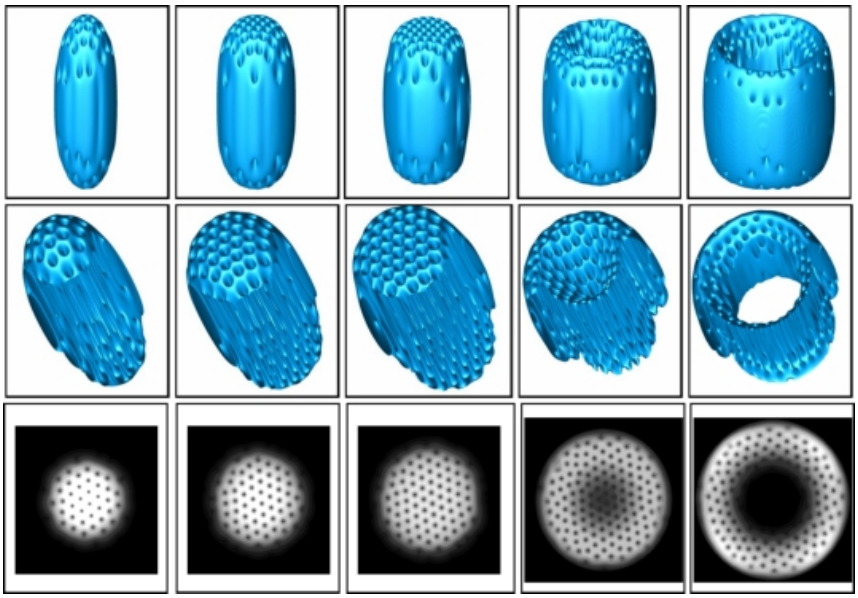

Figure 6.7.: Numerically generated condensates obtained using a *quartic-plus-quadratic* trapping potential with the parameters corresponding to experiments of Bretin et al. (2004). Equilibrium configurations for different rotation rates: from left to right, $\Omega/2\pi = 60, 64, 66, 70.6, 73$. Three-dimensional views of the vortex lattice identified by means of iso-surfaces of low atomic-density (top rows) and 2D views of the integrated density along the z-axis (lower row).

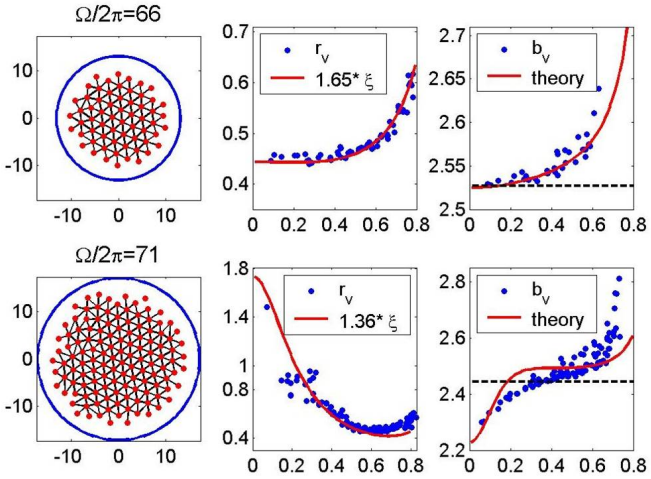

Figure 6.8.: Vortex lattice and variation of vortex core radius r_v and inter-vortex spacing b_v (values in μm) as functions of the non-dimensional radius $r/R_\perp$. Quantitative data extracted from numerical simulations. Comparison with theoretical predictions (solid lines) of Sheehy and Radzihovsky (2004).

6.3. Vortices with exotic shapes in non-rotating BECs

The new phase-engineering capabilities, recently developed by the MIT group (Leanhardt et al., 2002), open many possibilities for the generation of topological defects. This makes very interesting the question of finding theoretical methods for the design of new types of vortices. We have imagined in Crasovan et al. (2004) some original vortex shapes that could be obtained in non-rotating condensates by phase-imprinting. We show that the spatial structure of the wave function of the condensate with *exotic* vortices can be written as:

$$\psi(x,y,z) = \phi(x,y,z)e^{-\sum_{k=x,y,z}\lambda_k x_k^2/2}, \tag{6.3.1}$$

where ϕ is a polynomial form resulting from the combination of Hermite polynomials. We can obtain a rich variety of vortices:

- vortex stars (Fig. 6.9a) described by

$$\begin{aligned}\phi_{\text{star}} &= H_2(x)H_0(y)H_0(z) - H_0(x)H_2(y)H_0(z)\\ &+ i(H_2(x)H_0(y)H_0(z) - H_0(x)H_0(y)H_2(z))\\ &= 4\left[(x^2-y^2)+i(x^2-z^2)\right].\end{aligned} \tag{6.3.2}$$

- pairs of parallel vortex rings (Fig. 6.9b)

$$\begin{aligned}\phi_{\parallel} &= H_2(x)H_0(y)H_0(z) + H_0(x)H_2(y)H_0(z)\\ &+ H_0(x)H_0(y)H_2(z) + iH_0(x)H_0(y)H_2(z)\\ &= \left[(4x^2+4y^2+4z^2-6)+i(4z^2-2)\right]\end{aligned} \tag{6.3.3}$$

- pairs of perpendicular vortex rings (Fig. 6.9c)

$$\begin{aligned}\phi_{\perp} &= H_2(x)H_0(y)H_0(z) + H_0(x)H_2(y)H_0(z)\\ &+ H_0(x)H_0(y)H_2(z) + iH_1(x)H_1(y)H_0(z)\\ &= \left[(4x^2+4y^2+4z^2-6)+4ixy\right],\end{aligned} \tag{6.3.4}$$

- antiparallel vortex lines (Fig. 6.9d)

$$\begin{aligned}\phi(x,y,z) &= H_2(x)H_0(\sqrt{2}y) + iH_0(x)H_1(\sqrt{2}y)\\ &= 4x^2 - 2 + 2i\sqrt{2}y\end{aligned} \tag{6.3.5}$$

- stationary n-vortex rings (Fig. 6.9e, for $n = 1$)

$$\begin{aligned} \phi(x,y,z) &= H_0\left(\sqrt{2/n}\ z\right)\left[H_2(x)H_0(y) + H_0(x)H_2(y)\right] \\ &+ iH_0(x)H_0(y)H_n\left(\sqrt{2/n}\ z\right) \\ &= 4(x^2+y^2-1) + iH_n\left(\sqrt{2/n}\ z\right). \end{aligned} \tag{6.3.6}$$

For the configurations (a, b, c) we set $\lambda_x = \lambda_y = \lambda_z = 1$ and for the cases (d, e) $\lambda_x = \lambda_z = 1$ and $\lambda_y = 2$. A very important question we have answered is the stability of these stationary states. Numerical (real and imaginary time) simulations showed that they are robust excited states that could last in BECs for long times.

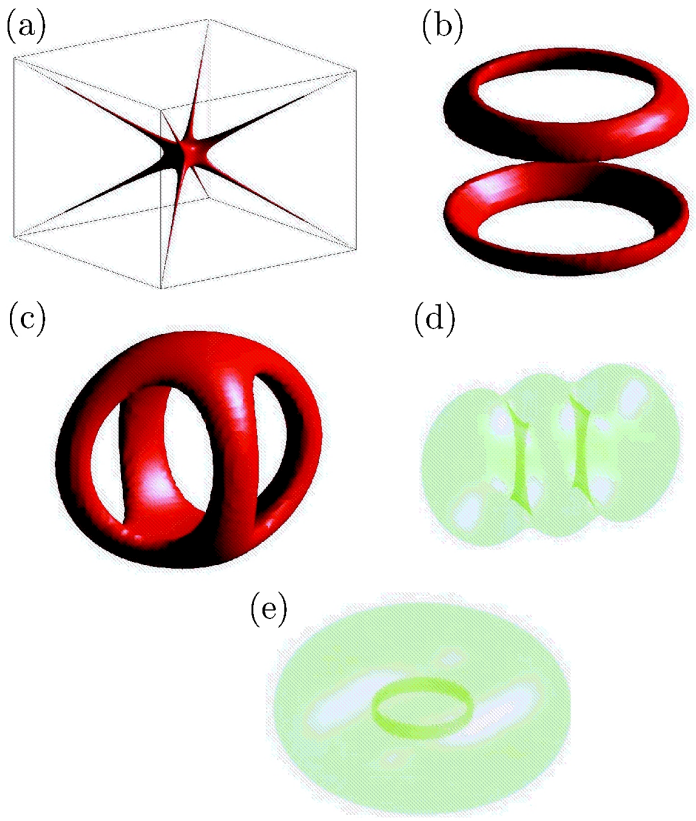

Figure 6.9.: Theoretical *exotic* vortex shapes that could be obtained in a non-rotating BEC by phase-engineering techniques (Crasovan et al., 2004).

7. Work in progress and future plans

Future work concerning the numerical investigation of Bose-Einstein condensates will focus on two main topics: rotating BECs in optical lattices and development of new numerical schemes for BEC simulations.

7.1. Mathematical and numerical study of a BEC in 1D optical lattices

New experiments performed by the ENS group (Hadzibabic et al., 2004) consider a prolate (cigar-shaped) condensate placed in an 1D optical lattice directed along the z-axis. The modified trapping potential is for this case:

$$V(r,z) = V_h(r,z) + U_s \sin^2(\pi z/d),$$

where $V_h(r,z)$ is the *classical* harmonic potential (5.2.2). For large values of the amplitude U_s, the initial condensate is divided in several sites, depending on the value of the parameter d. In experiments, 30 to 32 sites are obtained, but they are difficult to distinguish in pictures, as shown in Fig. 7.1.

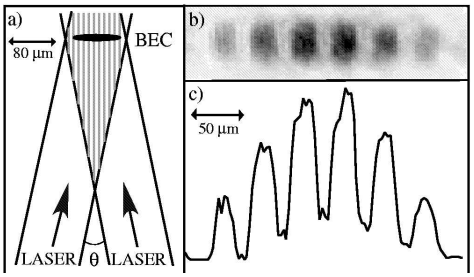

Figure 7.1.: Non-rotating BEC in 1D optical lattice. Experimental visualization (Hadzibabic et al., 2004).

Three-dimensional simulations are compulsory for the study of such systems. I have recently considered similar configurations, but with the condensate in rotation. Preliminary numerical results (Fig. 7.2) show a large variety of arrangements of vortex lattices, different from one site to another, and strongly depending on the rotation frequency and the amplitude of the optical lattice. Since experimental data are not yet available for such rotating configuration, these numerical simulations will contribute to the theoretical description of new phenomena in rotating BECs.

Theoretical and numerical analysis of such systems will first focus on configurations with two or three sites. Numerical results for these cases are already available.

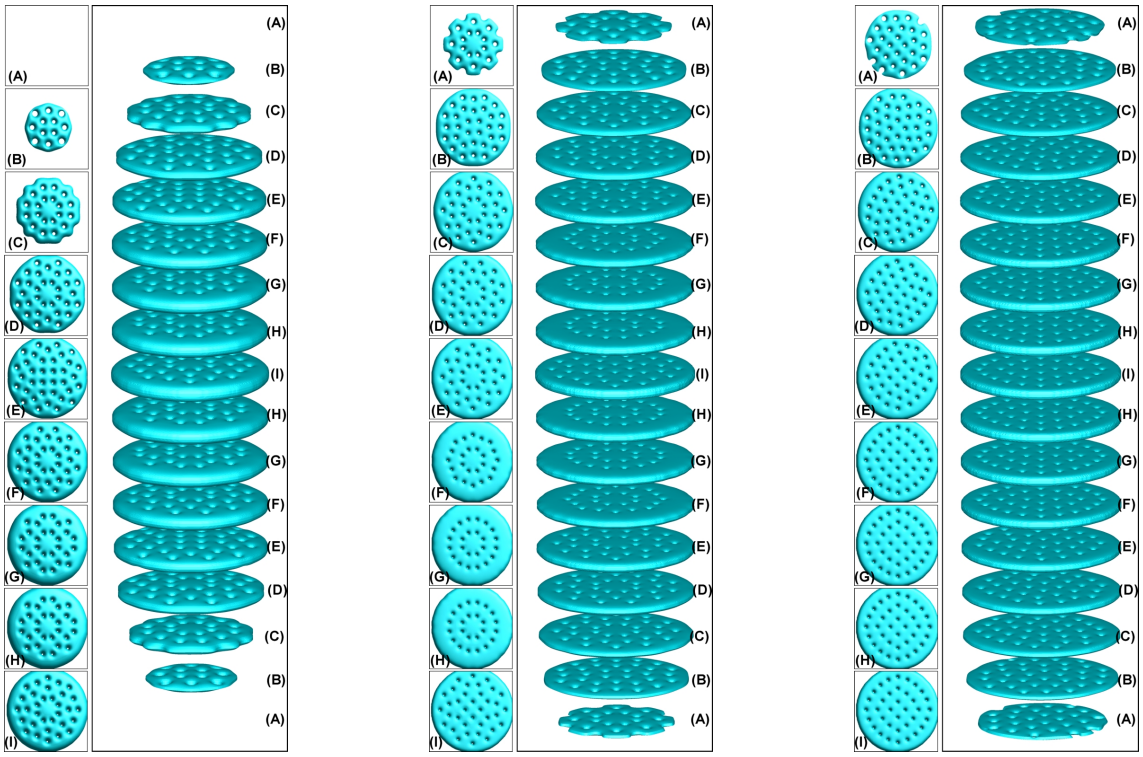

Figure 7.2.: Rotating cigar-shape condensate placed in an 1D optical lattice along the longitudinal z-axis. The rotation frequency is the same for the three (converged) configurations. The amplitude U_s of the optical lattice increases from left to right.

The mathematical analysis of this problem is the main topic of the post-doctoral research that Parimah Kazemi, (PhD from North Texas University) will start in October in our laboratory. I shall co-advise this post-doc together with Sylvia Serfaty (Professor, Paris 6).

7.2. Numerical development of the code BETI

Numerical simulations of condensates in optical lattices request large spatial grids and, consequently, large computational time. Future work on the numerical code BETI will include the optimization of the numerical schemes and the development of a parallel version of the code. This is not an easy task since several implicit schemes are used in the code (compact schemes, Crank-Nicolson time integration).

A new version of the code using cylindrical coordinates is currently under development. The extension for the *real-time* simulation using methods described in Bao and Du (2006) is also planned.

III

Bibliography

Bibliography of chapter 1

I. Danaila. *Etude des instabilités et des structures cohérentes dans la zone de proche sortie d'un jet axisymétrique*. PhD thesis, Université d'Aix–Marseille II, 1997.

I. Danaila and B. J. Boersma. Mode interaction in a forced homogeneous jet at low Reynolds numbers. In *Proceedings of the Summer Program*, page 141. Center for Turbulence Research, Stanford Univ., 1998.

I. Danaila and B. J. Boersma. Direct numerical simulation of bifurcating jets. *Physics of Fluids*, 12:1255–1257, 2000.

I. Danaila, J. Dusek and F. Anselmet. Space Structure of the Free, Unsteady, Round, Homogeneous Jet at Low Reynolds Numbers. In L. Machiels S. Gavrilakis and P. A. Monkewitz, editors, *Advances in Turbulence VI*, pages 11–14. Kluwer Academic Publishers, 1996a.

I. Danaila, J. Dusek and F. Anselmet. Coherent structures in a round, spatially evolving, unforced, homogeneous jet at low Reynolds numbers. *Physics of Fluids*, 9:3323–3342, 1997a.

I. Danaila, J. Dusek and F. Anselmet. Direct numerical simulations of the free, unsteady, round, unforced jet at low Reynolds numbers. In P. R. Voke J.-P. Chollet and L. Kleiser, editors, *Direct and Large–Eddy Simulation II*, pages 1–10. Kluwer Academic Publishers, 1997b.

I. Danaila, J. Dusek and F. Anselmet. Coherent structures in a round, spatially evolving, unforced, homogeneous jet at low Reynolds numbers. *Physical Review E*, 57:3695–3698, 1998a.

I. Danaila, J. Dusek and F. Anselmet. Nonlinear dynamics of Low Reynolds Number Round Jets: Periodic Attractors and Transition to Chaos. In U. Frisch, editor, *Advances in Turbulence VII*, pages 105–108. Kluwer Academic Publishers, 1998b.

G. Carte, J. Dušek and Ph. Fraunié. A spectral time discretization for flows with dominant periodicity. *J. Comput. Physics*, 120:171, 1995.

P. Durbin and B. Pettersson Reif. *Statistical Theory and Modeling of Turbulent Flows*. John Wiley & Sons, Chichester, New York, 2000.

J. Dušek, P. Le Gal and Ph. Fraunié. A numerical and theoretical study of the first Hopf bifurcation in a cylinder wake. *J. Fluid Mech.*, 264:59, 1994.

R. D. Henderson and G. EM Karniadakis. Unstructured spectral element methods for simulation of turbulent flows. *J. Comput. Physics*, 122:191, 1995.

A. Hilgers and B. J. Boersma. Optimization of turbulent jet mixing. *Fluid Dyn. Res.*, 29:345, 2001.

G. M. Homsy. *Multimedia Fluid Mechanics, 2nd edition.* Cambridge University Press, Cambridge, New York, 2008.

M. Lee and W. C. Reynolds. *Bifurcating and blooming jets.* Rep. tf–22, Dep. Mech. Eng. Thermosci. Div., Stanford Univ., 1985.

G. P. Neitzel, C. S. Kirkconnell and L. J. Little. Transient, nonaxisymmetric modes in the instability of unsteady circular Couette flow. Laboratory and numerical experiments. *Phys. Fluids*, 7:324, 1995.

D. Parekh, A. Leonard and W. C. Reynolds. *Bifurcating jets at high Reynolds numbers.* Rep. tf–35, Dep. Mech. Eng. Thermosci. Div., Stanford Univ., 1988.

A. T. Patera. A spectral element method for Fluid Dynamics: laminar flow in a channel expansion. *J. Comput. Physics*, 54:468, 1984.

W. C. Reynolds, D. E. Parekh, P. J. D. Juvet and M. J. D. Lee. Bifurcating and blooming jets. *Ann. Rev. Fluid Mech.*, 35:295, 2003.

H. Suzuki, N. Kasagi and Y. Suzuki. On the formation of vortex rings and pairs. *Experiments in Fluids*, 36:498, 2004.

M. Van Dyke. *Perturbation method in fluid mechanics.* Stanford: The Parabolic Press, Stanford, California, 1975.

Bibliography of chapter 2

C. M. Albone. Embedded meshes of controllable quality synthesised from elementary geometric features. *AIAA Paper*, 92:0662, 1992.

P. Angot, C.-H. Bruneau and P. Fabrie. A penalization method to take into account obstacles in incompressible viscous flows. *Numerische Mathematik*, 81: 497, 1999.

I. Danaila. *Numerical implementation of the body–force method in the NTMIX Code.* Rapport interne, Institut Français du Pétrole, 2001.

I. Danaila. Vortex dipoles impinging on finite aspect ratio rectangular obstacles. *Flow, Turbulence and Combustion*, 72:391, 2004.

I. Danaila and T. Baritaud. *Large Eddy Simulations for Stratified Charge Engines. LES Engines Program. Twelve–months periodic report.* Rapport interne, Institut Français du Pétrole, 1999.

I. Danaila and S. Benteboula. *Etude numérique et théorique des structures tourbillonnaires dans une injection gaz–gaz. Simulations numériques directes avec les codes JETLES et AVBP.* Rapport de contrat, Paris 6 et Institut Français du Pétrole, 2004.

O. El Ganaoui, C. Habchi, G. Bruneaux and I. Danaila. Numerical simulation of an experimental gas–gas jet generated by single–hole diesel–like injection. *Int. J. Numer. Meth. Fluids*, 47:1011–1018, 2005.

H. Lamb. *Hydrodynamics*. Dover, New York, 1932.

S. K. Lele. Compact finite difference schemes with spectral–like resolution. *J. Comput. Physics*, 103:16, 1992.

S. Maurel, J. Borée and J.L. Lumley. Extended proper orthogonal decomposition: application to jet/vortex interaction. *Flow, Turbulence and Combustion*, 67:125, 2001.

R. Mittal and G. Iaccarino. Immersed boundary method. *Ann. Rev. Fluid Mech.*, 37:239, 2005.

J. Mohd-Yosuf. Combined immersed boundary/B–spline methods for simulation of flow in complex geometries. *Annu. Res. Briefs, Cent. Turbul. Res.*, page 317, 1997.

P. Orlandi and R. Verzicco. Vortex Rings Impinging on Walls: Axisymmetric and Three–Dimensional Simulations. *J. Fluid Mech.*, 256:615, 1993.

T. Poinsot and S. K. Lele. Boundary conditions for direct simulations of compressible viscous flows. *J. Comput. Physics*, 101:104, 1992.

E. M. Saiki and S. Biringen. Numerical simulation of a cylinder in uniform flow: application of a virtual boundary method. *J. Comput. Physics*, 123:450, 1996.

T. Schönfeld and M. Rudgyardt. Steady and unsteady flow simulations using the hybrid flow solver AVBP. *AIAA Journal*, 37:1378, 1999.

J. L. Steger, F. C. Dougherty and J. A. Benek. A Chimera grid scheme. In *Advances in grid generation*, page 59. ASME FED–5, 1983.

Bibliography of chapter 3

M. Ballestra. *Etude numérique de la formation et la dissipation des tourbillons créé par un jet conique monophasique.* Rapport de stage de DESS de mathématiques appliquées, Université Paris 6, 2002.

G. K. Batchelor. *An Introduction to Fluid Dynamics.* Cambridge University Press, Cambridge, New York, 7th edition, 1988.

S. Benteboula. *Résolution des équations de Navier–Stokes à faible nombre de Mach : Application à l'étude de l'anneau tourbillonnaire à masse volumique variable.* PhD thesis, Université de Marne–la–Vallée, 2006.

S. Benteboula and I. Danaila. Simulation numérique de l'injection gaz–gaz à masse volumique variable. *Congrès Français de Thermique*, 2006.

S. Benteboula and I. Danaila. Variable density vortex rings. In J. M. L. M. Palma and A. Silva Lopes, editors, *Advances in Turbulence XI*, page 771. Springer, 2007.

I. Danaila. *Code JETLES. Simulations numériques directes (DNS) et des grandes échelles (LES) des écoulements incompressibles en coordonnées cylindriques.* documentation du code jetles, Paris 6, 1999–2008.

I. Danaila and S. Benteboula. *Etude numérique et théorique des structures tourbillonnaires dans une injection gaz–gaz. Simulations numériques directes avec les codes JETLES et AVBP.* Rapport de contrat, Paris 6 et Institut Français du Pétrole, 2004.

I. Danaila and J. Hélie. Numerical simulation of the postformation evolution of a laminar vortex ring. *Phys. Fluids*, 20:073602, 2008.

A. W. Cook and J. J. Riley. Direct numerical simulation of a turbulent reactive plume on a parallel computer. *J. Comput. Physics*, 129:263–283, 1996.

J. O. Dabiri and M. Gharib. Fluid entrainment by isolated vortex rings. *J. Fluid Mech.*, 511:311–331, 2004.

M. Gharib, E. Rambod and K. Shariff. A universal time scale for vortex ring formation. *J. Fluid Mech.*, 360:121–140, 1998.

F. B. Kaplanski and Y. A. Rudi. A model for the formation of "optimal" vortex ring taking into account viscosity. *Phys. Fluids*, 17:087101, 2005.

J. Kim and P. Moin. Application of a fractional step method to incompressible Navier–Stokes equations. *J. Comput. Physics*, 59:308–323, 1985.

O.M. Knio, P.S. Worlikar and Najm H. N. Conservative high–order finite–difference scheme for low–Mach number flows. *J. Comput. Physics*, 158:71–97, 2000.

A. Majda and J. Sethian. The derivation and numerical solution of the equation for zero Mach number combustion. *Combust. Sci. Technol.*, 42:185, 1985.

H. K. Moffatt. Generalised vortex rings with and without swirl. *Fluid Dyn. Res.*, 3:22–30, 1988.

P. Orlandi. *Fluid Flow Phenomena: A Numerical Toolkit*. Kluwer Academic Publishers, Dordrecht, 1999.

M. Rai and P. Moin. Direct Simulations of Turbulent Flow Using Finite–Difference Schemes. *J. Comput. Physics*, 96:15–53, 1991.

P. G. Saffman. *Vortex Dynamics*. Cambridge University Press, Cambridge, New York, 1992.

K. Shariff and A. Leonard. Vortex rings. *Ann. Rev. Fluid Mech.*, 24:235–279, 1992.

R. Verzicco and P. Orlandi. A finite–difference scheme for three–dimensional incompressible Flows in cylindrical coordinates. *J. Comput. Physics*, 123:402–414, 1996.

C. B. Vreugenhil and B. Koren. *Numerical methods for advection–diffusion problems*, volume 45. Vieweg, Braunschweig, 1993.

Bibliography of chapter 4

H. Berestycki, E. Fernandez Cara and R. Glowinski. A numerical study of some questions invortex ring theory. *RAIRO Analyse numérique*, 18:7–85, 1984.

I. Danaila and J. Hélie. Numerical simulation of the postformation evolution of a laminar vortex ring. *Phys. Fluids*, 20:073602, 2008.

J. Blum, C. Boulbe and B. Faugeras. Real time reconstruction of plasma equilibrium in a Tokamak. In *International Conference on burning plasma diagnostics, Villa Monastero, Varenna*, 2007.

D. Das and J. H. Arakeri. Transition of unsteady velocity profiles with reverse flow. *J. Fluid Mech.*, 374:251–283, 1998.

F. Durst, B. Schönung and M. Simons. Steady ellipsoidal vortex rings with finite cores. *Journal of Applied Mathematics and Physics (ZAMP)*, 32:0156, 1981.

M. J. Esteban. Nonlinear elliptic problems in strip–like domains: symmetry of positive vortex rings. *Nonlinear Analysis, Theory, Methods & Applications*, 7: 365–379, 1983.

D. Fargie and B. W. Martin. Developing laminar flow in a pipe of circular cross–section. *Proceedings of the Royal Society of London. Series A, Mathematical and Physical Sciences*, 321:461–476, 1971.

L. E. Fraenkel and M. S. Berger. A global theory of steady vortex rings in an ideal fluid. *Acta Math.*, 132:13–51, 1974.

P. M. Gresho and R. L. Sani. *Incompressible Flow and the Finite Element Method, vol. 2.* Wiley, New York, 2000.

J. Norbury. A family of steady vortex rings. *J. Fluid Mech.*, 57:417, 1973.

O. Pironneau and P. M. Gresho. Authors reply. *Int. J. Numer. Meth. Fluids*, 56:1966, 2008.

R. L. Sani, J. Shen, O. Pironneau and P. M. Gresho. Pressure boundary condition for the time–dependent incompressible Navier.Stokes equations. *Int. J. Numer. Meth. Fluids*, 50:673–682, 2006.

Bibliography of chapter 5

J. R. Abo-Shaeer, C. Raman, J. M. Vogels and W. Ketterle. Observation of Vortex Lattices in Bose-Einstein Condensates. *Science*, 292:476, 2001.

A. Aftalion. *Vortices in Bose-Einstein Condensates.* Birkhauser, 2006.

A. Aftalion and Q. Du. Vortices in a rotating Bose-Einstein condensate: Critical angular velocities and energy diagrams in the Thomas-Fermi regime. *Phys. Rev. A*, 64:063603, 2001.

A. Aftalion and R. L. Jerrard. Shape of vortices for a rotating Bose Einstein condensate. *Phys. Rev. A*, 66:023611, 2002.

A. Aftalion and T. Riviere. Vortex energy and vortex bending for a rotating Bose-Einstein condensate. *Phys. Rev. A*, 64:043611, 2001.

W. Bao and Q. Du. Computing the ground state solution of Bose-Einstein condensates by a normalized gradient flow. *Siam J. Sci. Comput.*, 25:1674, 2004.

W. Bao and Q. Du. Dynamics of rotating Bose-Einstein condensates and its efficient and accurate numerical computation. *Siam J. Appl. Math.*, 66:758, 2006.

N. G. Berloff. Interactions of vortices with rarefaction solitary waves in a Bose-Einstein condensate and their role in the decay of superfluid turbulence. *Phys. Rev. A*, 69:053601, 2004.

J. J. García-Ripoll and V. M. Pérez-García. Vortex bending and tightly packed vortex lattices in Bose-Einstein condensates. *Phys. Rev. A*, 64:053611, 2001.

K. Kasamatsu, M. Machida, N. Sasa and M. Tsubota. Three-dimensional dynamics of vortex-lattice formation in Bose-Einstein condensates. *Phys. Rev. A*, 71:063616, 2005.

S. K. Lele. Compact finite difference schemes with spectral-like resolution. *J. Computational Physics*, 103:16, 1992.

K. W. Madison, F. Chevy, V. Bretin and J. Dalibard. Stationary States of a Rotating Bose-Einstein Condensate: Routes to Vortex Nucleation. *Phys. Rev. Lett.*, 86:4443, 2001.

K. W. Madison, F. Chevy, W. Wohlleben and J. Dalibard. Vortex Formation in a Stirred Bose-Einstein Condensate. *Phys. Rev. Lett.*, 84:806, 2000.

M. Modugno, L. Pricoupenko and Y. Castin. Bose-Einstein condensates with a bent vortex in rotating traps. *European Physical Journal D*, 22:0203597, 2003.

C. Raman, M. Köhl, R. Onofrio, D. S. Durfee, C. E. Kuklewicz, Z. Hadzibabic and W. Ketterle. Evidence for a Critical Velocity in a Bose-Einstein Condensed Gas. *Phys. Rev. Lett.*, 83:2502, 1999.

Bibliography of chapter 6

A. Aftalion. *Vortices in Bose-Einstein Condensates*. Birkhauser, 2006.

A. Aftalion and I. Danaila. Three-dimensional vortex configurations in a rotating Bose Einstein condensate. *Physical Review A*, 68:023603, 2003.

A. Aftalion and I. Danaila. Giant vortices in combined harmonic and quartic traps. *Physical Review A*, 69:033608, 2004.

A. Aftalion and T. Riviere. Vortex energy and vortex bending for a rotating Bose-Einstein condensate. *Phys. Rev. A*, 64:043611, 2001.

I. Danaila. Three-dimensional vortex structure of a fast rotating Bose-Einstein condensate with harmonic-plus-quartic confinement. *Physical Review A*, 72:013605(1–6), 2005.

V. Bretin. *Rotations d'un condensat de Bose-Einstein*. PhD thesis, Université Paris 6, 2004.

V. Bretin, S. Stock, Y. Seurin and J. Dalibard. Fast Rotation of a Bose-Einstein Condensate. *Phys. Rev. Lett.*, 92:050403, 2004.

L.-C. Crasovan, V. M. Pérez-Garcìa, I. Danaila, D. Mihalache and L. Torner. Three-dimensional parallel vortex rings in Bose-Einstein condensates. *Physical Review A*, 70:033605, 2004.

J. K. Kim and A. L. Fetter. Dynamics of rapidly rotating Bose-Einstein condensates in a harmonic plus quartic trap. *Phys. Rev. A*, 72:023619, 2005.

A. E. Leanhardt, A. Görlitz, A. P. Chikkatur, D. Kielpinski, Y. Shin, D. E. Pritchard and W. Ketterle. Imprinting Vortices in a Bose-Einstein Condensate using Topological Phases. *Phys. Rev. Lett.*, 89:190403, 2002.

K. W. Madison, F. Chevy, V. Bretin and J. Dalibard. Stationary States of a Rotating Bose-Einstein Condensate: Routes to Vortex Nucleation. *Phys. Rev. Lett.*, 86:4443, 2001.

P. Rosenbusch, V. Bretin and J. Dalibard. Dynamics of a Single Vortex Line in a Bose-Einstein Condensate. *Phys. Rev. Lett.*, 89:200403, 2002.

D. E. Sheehy and L. Radzihovsky. Vortices in spatially inhomogeneous superfluids. *Phys. Rev. A*, 70:063620, 2004.

S. Stock, B. Battelier, V. Bretin, Z. Hadzibabic and J. Dalibard. Bose-Einstein condensates in fast rotation. *Laser Physics Letters*, 2:275, 2005.

Bibliography of chapter 7

W. Bao and Q. Du. Dynamics of rotating Bose-Einstein condensates and its efficient and accurate numerical computation. *Siam J. Appl. Math.*, 66:758, 2006.

Z. Hadzibabic, S. Stock, B. Battelier, V. Bretin and J. Dalibard. Interference of an array of independent Bose-Einstein condensates. *Phys. Rev. Lett.*, 93: 180403, 2004.